6-2008

Optical Emissions Generated During Ionospheric Heating

Charles Kiumo Mutiso
Embry-Riddle Aeronautical University - Daytona Beach

Optical Emissions Generated During Ionospheric Heating

A thesis submitted to the Physical Science Department

in partial fulfillment of the requirements for the

Degree of

Master of Science in Space Science

by

Charles Kiumo Mutiso

EMBRY-RIDDLE AERONAUTICAL UNIVERSITY

Daytona Beach, Florida

June 2008

Thesis Committee:

Dr. B. M. Hughes, Chair

Dr. G. G. Sivjee

Dr. M. A. Reynolds

Dr. P Erdman

Dr. P. Erdman, Program Coordinator, MSSPS

Dr. J. J. Olivero, Department Chair

Dr. J. Cunningham, Associate Provost

June 2008

Nomenclature

χ	angle between vertical and the magnetic field orientation
ϵ_o	permittivity of free space
ν	frequency
ϕ_c	Spitze angle
e	charge of an electron
f_h	heater frequency
f_oF_2	ionospheric critical frequency
f_p	plasma frequency
f_{ce}	electron cyclotron frequency
f_{uh}	upper hybrid frequency
h	Planck's constant
Kp	geomagnetic index
m_e	mass of an electron
m_i	mass of an ion

n_e	electron density
B	magnetic field vector
CCD	charge-coupled device
CW	continuous wave, a radio wave of constant amplitude and frequency
ERP	effective radiated power
FWHM	full width at half maximum
HF	high-frequency
ISR	incoherent scatter radar
O(^1D)	oxygen emission at 630.0 nm
O(^1S)	oxygen emission at 557.7 nm
O($^3D^o$)	oxygen emission at 799.0 nm
O(^3P)	oxygen emission at 844.6 nm
O(^5P)	oxygen emission at 777.4 nm
O^+	emission from ionized oxygen at 732.0−733.0 nm
o-mode	ordinary mode, a wave polarized such that the rotation of the electric field vector is opposite the electron cyclotron motion
PDI_L	parametric decay instability of Langmuir waves
$PDI_{EB/UH}$	parametric decay instability of electron Bernstein/upper hybrid waves
PRL	plasma resonance layer

RIOE	radio-induced optical emission
S/N	signal-to-noise ratio
TPI_{UH}	thermal parametric instability of upper hybrid waves
UHF	ultrahigh-frequency
UHRL	upper hybrid resonance layer
up-**B**	up the local magnetic field line
x-mode	extraordinary mode, a wave polarized such that the rotation of the electric field vector is in the same sense as the electron cyclotron motion

Abstract

Ionospheric heating, accomplished by transmitting a high-frequency electromagnetic wave into the atmosphere, stimulates a large number of linear and non-linear wave-plasma interactions. One outcome of these interactions is the acceleration of thermal ionospheric electrons, leading to the production of induced optical emissions. Detection of these emissions yields information regarding wave-plasma interactions, which are of fundamental importance in many physical processes, and provides an effective means of remotely sensing ionospheric constituents and dynamics.

During an ionospheric heating experiment performed at the High Power Auroral Stimulation facility in Alaska (64.9° N, 146.8° W), a modified Czerny-Turner grating spectrometer acquired high resolution optical spectra of a heated volume. In addition to the already-documented O(^3P) 844.6 nm (excitation energy of 10.99 eV), and O(^5P) 777.4 nm (10.74 eV) emissions, two previously unreported radio-induced optical emissions, O^+ 732−733 nm (18.61 eV), and O($^3D^o$) 799.0 nm (12.49 eV), were observed. The experiment utilized a 2.85 MHz, 32 MW effective radiated power, o-mode radio wave, pointed into the magnetic zenith.

This thesis presents the first spectroscopic time series observations of a heated volume, showing optical emission modulation by the heater, and summarizes the current state of high-latitude ionospheric heating, with a focus on the generation and detection of optical emissions.

Acknowledgments

Above all, I thank God for blessing me beyond measure.

I am grateful to my parents, Mommy and Baba, for raising me in relative comfort, for instilling in me values that prepared me to face life, and for giving me the freedom and ability to pursue whatever I set my mind to. Tosh and Munyaks, you deserve mention, because apart from being my siblings, you have inspired, guided, and looked out for me.

My pastor, David Flowers, is a man I count myself very fortunate of knowing. I am thankful for the love, guidance and support that he and his family have shown me. The same goes for my church family.

I am indebted to all my coworkers in the Space Physics Research Lab for sharing their knowledge with me. A large debt of gratitude is owed to John Pesce, for his endless patience and unselfish, constant willingness to answer my questions. I also have to thank Susan Adams, who has overseen the lab's administrative duties, thereby freeing me to concentrate on my research.

Sincere thanks must be directed to all teachers who have instructed me. Teaching is not easy, and the sacrifices teachers make often go unacknowledged. My thesis committee consists of teachers who deserve special mention: Dr Reynolds, whose Classical Mechanics course showed me just how little I knew, and Dr Erdman, in whose class I found out that even the little I thought I knew, I did not know as well

as I thought I did. I am especially appreciative of Dr Sivjee, for getting me started in this field, for his more than generous financial and professional support during my time at the Space Physics Research Lab, and for six challenging but educational Physics classes. He sets a high standard for pedagogy and experimental excellence.

My committee chair, Dr Hughes, is a pretty cool guy. Possessive of a sharp mind, a great sense of humor, and an easy-going personality, he is a big inspiration. It has been a joy working under him. Thanks for the good times, Dr Hughes.

Last but not least, to all my friends and extended family, know that you are all appreciated.

Charles Mutiso

9 June 2008

Contents

Figures

Tables

Outline

This thesis presents spectroscopic observations of artificially induced aurora, detected during an ionospheric heating experiment. The motivation for studying artificially induced and natural aurora is the same: to better understand the complex physical and chemical processes governing the interaction of the Sun with our planet.

To put the observations in context, a large portion of this work is devoted to introductory material. Chapter 1 briefly reviews the ionosphere, touching on its composition and vertical structure. Next, the auroral phenomenon is explored. The causes, extent and important emissions of the aurora are presented. Chapter 2 introduces concepts associated with radio wave propagation in the ionosphere. This sets the stage to offer a brief overview of ionospheric heating, focusing on the generation and detection of radio-induced optical emissions (RIOEs) at high latitudes.

Chapter 3 describes the instrumentation, consisting of the ionospheric heater and the optical spectrometer. Details regarding the experiment conditions and data analysis are provided. Subsequently, Chapter 4 presents the main results: spectra and time series of the optical emissions generated during the heating experiment. The relevance of the findings from this work is discussed in the context of previous experiments. A summary and a plan for future work conclude this thesis.

Chapter 1

Background

"Easy cake."
Dr R

1.1 The ionosphere

Plasma comprises more than 99% of all known matter in the universe. The ionized, quasi-neutral component of Earth's upper atmosphere, the ionosphere, forms the nearest appreciable concentration of plasma. Extending from roughly 60 to 600 km in altitude, the ionosphere contains an approximately equal number of free electrons and positively charged ions. At an altitude of 250 km, there are about 10^{11} charged particles and 10^{15} neutral atoms and molecules per m^3. Although the charged particles are several orders of magnitude less abundant than the neutrals, they play a significant role in determining the physical and chemical characteristics of the ionosphere.

Figure 1.1 presents the neutral composition of the atmosphere. Major constituents at lower altitudes include N_2, O_2, and O (atomic oxygen). Between 200−600 km, O forms the bulk of the ionosphere, while at higher altitudes, hydrogen and helium are more abundant. Above the turbopause, at ~100 km, the constituents are not well mixed, and separate due to gravity. Lighter atoms exhibit the smallest change in

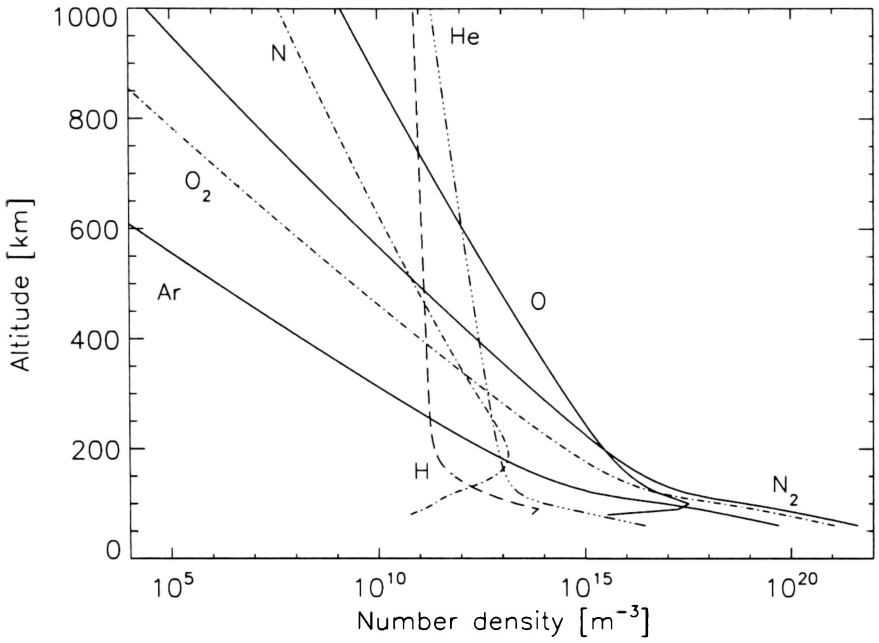

Figure 1.1: Typical composition of the high-latitude neutral atmosphere at close to solar minimum, showing the main constituents. (From the MSIS-E-90 atmospheric model at *http://omniweb.gsfc.nasa.gov/vitmo/msis_vitmo.html*)

density per unit altitude.

Figure 1.2 shows the net concentration of free electrons, termed the electron density, n_e, in the mid-latitude ionosphere. The electron density is plotted as a function of altitude; there is a clear diurnal variation and a solar cycle dependence. The relative concentration of free electrons gives rise to the different ionospheric layers summarized in Table 1.1. Factors such as solar zenith angle, solar activity, latitude, and season affect the formation, altitude, and extent of the layers.

The ionosphere is formed principally by solar radiation and energetic particles ionizing neutral constituents of the upper atmosphere. Ionizing radiation intensifies with altitude, whereas the concentration of the ionizable neutrals decreases with

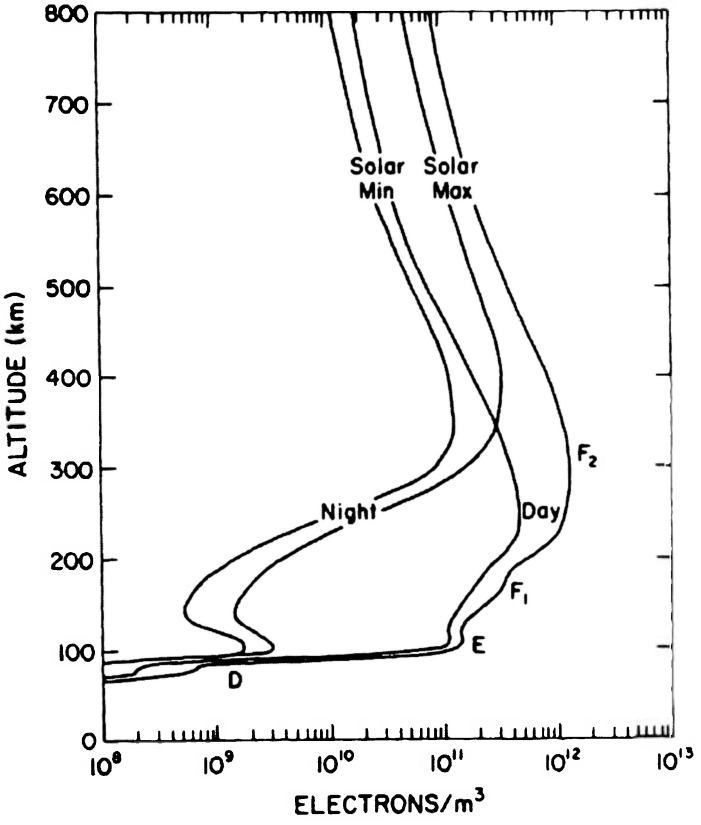

Figure 1.2: Mid-latitude electron density profiles for solar maximum and minimum. Diurnal variation is also evident. (Figure from *Rees* [1989].)

altitude. It follows that the electron density varies with altitude and will peak at a certain height. This maximum occurs in the F_2 layer, which has the densest plasma in Earth's environment [*Baumjohann and Treumann*, 1997].

Ion and electron number densities in the ionosphere are displayed in Figure 1.3. In the D and E layers, O_2^+ and NO^+ are the principal ions; in contrast, O^+ is the dominant ion in the F layer. Photoionization of atomic oxygen produces O^+ in the F_2 layer:

$$O + h\nu \longrightarrow O^+ + e \tag{1.1}$$

Table 1.1: Typical characteristics of the various ionospheric layers.

Layer	Altitude [km]	n_e $[m^{-3}]$	Notes
D	60–90	10^8–10^{10}	Significant degree of radio wave absorption; layer vanishes at night.
E	105–160	$\sim 10^{11}$	At high latitudes, precipitating particles contribute to its formation.
F_1	160–180	10^{11}–10^{12}	Vanishes at night.
F_2	200–400	$\sim 10^{12}$	Highest electron densities; significant in radio propagation.

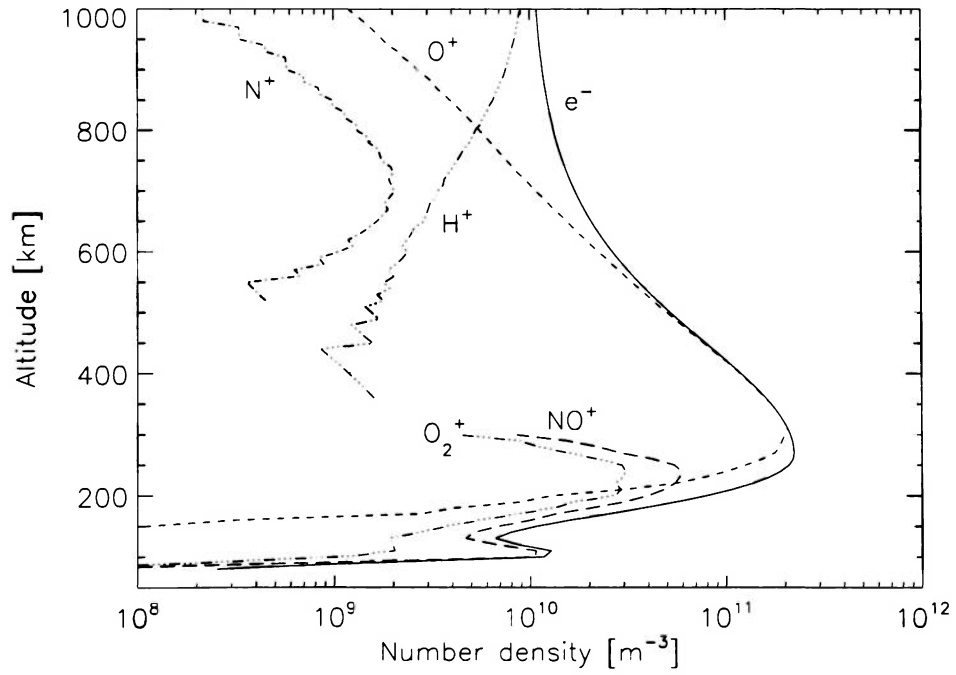

Figure 1.3: Typical ion composition and electron density profile of the high-latitude twilight ionosphere at close to solar minimum. (From the International Reference Ionosphere IRI-2001 at *http://modelweb.gsfc.nasa.gov/models/iri.html*)

O^+ ions are lost mainly through charge exchange reactions with O_2 and N_2 [*Gombosi*, 1998] according to

$$O^+ + O_2 \longrightarrow O_2^+ + O$$
$$O^+ + N_2 \longrightarrow NO^+ + N \qquad (1\ 2)$$

The O^+ number density thus depends on the relative rates of the production (equation 1 1) and loss (equations 1 2) processes Similarly, the abundance of ions and electrons is, to a large extent, a balance between photoionization and recombination Release of the absorbed solar energy via chemical reactions leads to the formation of airglow, the faint luminescence of the atmosphere At high latitudes, another phenomenon, the aurora, contributes to the sky brightness This is discussed next

1.2 Aurora

The eerie, majestic auroral lights[1] have captivated humans since long before we have been able to explain them These celestial wonders have been witnessed for millennia by the inhabitants of polar regions, yet it is only in the last half-century that significant progress has been made toward understanding them

Three conditions are necessary for the formation of aurora around a planet an atmosphere, a magnetic field, and a source of energetic charged particles All three are present on Earth, with the solar wind providing the majority of charged particles

The Sun's corona, at a temperature of over 1,000,000 K, is hot enough to break the molecular and atomic bonds of its main constituent, hydrogen Electrons and protons, comprising the bulk of the solar wind, are liberated and stream radially outward at an average speed of 450 km/s The solar wind has a density of ~6 particles per cm^3, and

[1]The word *aurora*, is Latin for "dawn," and in this work refers to emissions in the ultraviolet, visible, and infrared range of the electromagnetic spectrum

reaches the Earth after a travel time of roughly 4 days. Here, our planet's magnetic field prevents the direct penetration of solar wind particles into the atmosphere. However, entry is possible in the polar cusp regions (see Figure 1.4), which are characterized by open field lines that connect either with the interplanetary magnetic field (IMF) or the magnetosphere. Guided down the magnetic field lines, incoming charged particles with sufficient energy will precipitate into the ionosphere, imparting their energy to neutral and ionized atoms and molecules. Subsequent relaxation of the excited states is accompanied by the emission of photons of light, constituting the aurora. The cusp-entry process described above relates to the dayside aurora.

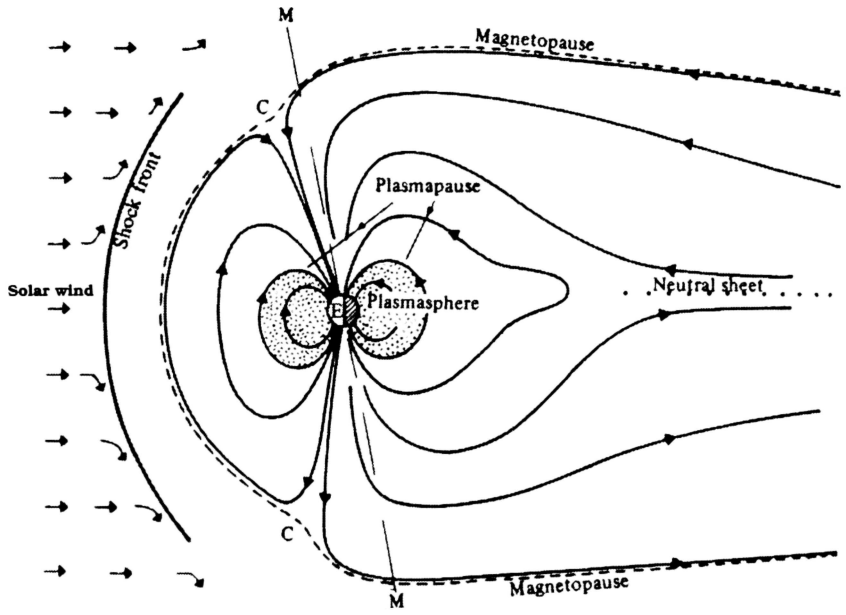

Figure 1.4: The open field lines of the high-latitude cusp regions, labeled C, allow direct entry of the solar wind plasma into Earth's ionosphere. MM is the magnetic polar axis. (From *Budden* [1985].)

On the nightside, reconnection and magnetospheric convection accelerate electrons to energies several orders of magnitude greater than on the dayside. Attendant with

this is precipitation of electrons to lower altitudes in the atmosphere. As will be shown later, the interaction altitudes and electron energies encountered during ionospheric heating are more similar to those observed on the dayside than on the nightside.

Auroras are thus footprints of the complex interactions between the solar wind and the Earth's ionosphere. The occurrence of auroras is generally limited to high-latitude bands asymmetric about the geographic poles, known as the auroral ovals (Figure 1.5). The location, shape and extent of the ovals vary significantly with solar activity, but on average they exhibit a maximum near 67° at midnight and 77° at noon (magnetic coordinates) [*Hunsucker and Hargreaves*, 2003]. Various auroral morphologies (poleward moving, sun-aligned, discrete, etc) and locations (dayside, nightside, cusp, pre/post noon), and their mapping to different processes (substorms, reconnection, flux transfer events) and magnetic field configurations (southward/northward IMF, radial IMF) are explored by *Sandholt et al.* [2002].

Numerous factors, such as particle flux and the energy spectra of the precipitating electrons, cause auroral displays to range in brightness, from sub-visual to bright enough to cast shadows. A quantitative measure of the brightness of an aurora is enabled by the unit Rayleigh [R]. If the surface brightness I of an aurora is measured in photons/cm^2/second/steradian, then the quantity $4\pi I$ gives the emission rate in photons/cm^2/second integrated in a column along the line of sight. One Rayleigh is thus defined as an apparent emission rate of 10^6 photons/cm^2/second/column [*Chamberlain*, 1961]. The "column" in the definition of the Rayleigh implies a dependence on the direction of observation: a large, diffuse auroral feature would be brighter if the line of sight was at a low elevation angle, compared to observing in the zenith direction. Typical auroral intensities range from 1 to 100 kR. For comparison, the light detection threshold of the dark-adapted human eye is about 1 kR of yellow-green light at ~550 nm [*Sandholt et al.*, 2002].

Figure 1.5: The northern hemisphere auroral oval during average geomagnetic conditions. The cross marks the North magnetic pole. (From *Gombosi* [1998].)

Given the large number of ionospheric constituents, each with multiple transitions radiating visible light, a multitude of emissions exist. Common auroral emissions and those pertinent to this work are summarized next.

1.2.1 Auroral emissions

The most common optical emissions in auroras result from transitions in atomic oxygen, which, as shown in Figure 1.1, is the dominant F-region constituent. The $O(^1D)$[‡] emission at 630.0 nm and the $O(^1S)$ at 557.7 nm can both be detected by

[‡]A word on notation: a superscript to the left of the letter is the quantity (2S+1), where S represents the total spin of the electrons; the letter stands for the total orbital angular momentum (S,P,D=0,1,2, respectively). A superscript "o" to the right of the letter indicates that the sum of the angular momentum over all the individual electrons is odd.

the human eye. The O(^1S) at 557.7 nm is the brightest and most common emission observed in the nightside aurora, and gives auroras their characteristic green color. The O(^1D) spectral line at 630.0 nm produces red photons and is also frequently detected, more on the dayside, where red auroras are prevalent. Both emissions have a relatively low excitation energy and are "forbidden" lines; their radiative transitions, governed by quantum-mechanical selection rules that favor electric-dipole transitions, have a low probability. Instead, electric-quadrupole and magnetic-dipole contributions allow for small but finite transition probabilities, implying long lifetimes (~seconds or minutes) for the excited states.

The O^+ 732–733 nm, O(^3P) 844.6 nm, O(^5P) 777.4 nm, and O($^3D^o$) 799.0 nm emissions and their auroral excitation mechanisms are discussed in the following sections. With the exception of O(^3P), these emissions are weaker and less readily observed than the red and green lines, due in part to their higher excitation energy. Table 1.2 lists typical intensities on the dayside. On the nightside, the higher electron energies and lower interaction altitudes yield different values.

Table 1.2: Typical intensities of several dayside auroral emissions.

Emission [nm]	Intensity [kR]	Reference
O(^1D) 630.0	1–10	*Sandholt et al.* [2002]
O(^1S) 557.7	0.1–1	*Sandholt et al.* [2002]
O(^3P) 844.6	0.2–3	*Christensen et al.* [1983]
O(^5P) 777.4	0.02–0.8	*Sivjee et al.* [1984]
O^+ 732.0	0.02–0.2	*Smith et al.* [1982]
O($^3D^o$) 799.0	0.015–0.4	*Christensen et al.* [1983]

1.2.2 O(^{1}S) 557.7 nm emission

The brightest single emission in airglow and aurora is the oxygen green line [*Chamberlain*, 1961; *Rees*, 1989], arising from:

$$O(^1S) \longrightarrow O(^1D) + h\nu \quad [557.7\ \text{nm}] \tag{1.3}$$

This is a forbidden transition, with a radiative lifetime of 0.74 seconds [*Chamberlain*, 1961]. The O(^1S) level is 4.17 eV higher than the ground state, and the primary source of excited atoms [*Rees*, 1989] is through:

$$N_2(A^3\Sigma_u^+) + O \longrightarrow N_2(X^1\Sigma_g^+) + O(^1S) \tag{1.4}$$

Gerdjikova and Shepherd [1987] and *Rees* [1989] also propose the following mechanisms as excitation sources of the auroral O(^1S) state:

$$O_2^+ + e \longrightarrow O + O(^1S) \tag{1.5}$$

$$O(^3P) + e \longrightarrow O(^1S) + e \tag{1.6}$$

The green line emanates from two distinct altitudes, one at 250−300 km, and a second at 95−100 km.

1.2.3 O(^{1}D) 630.0 nm emission

Three lines at 630.0, 636.4, and 639.2 nm are formed by the transition of the excited O(^1D) state to the triplet O(^3P) ground state, but the latter two are significantly weaker. The emission at 630.0 nm is prevalent in both the airglow and aurora, and has been extensively studied. A statistical lifetime of 110 seconds significantly

increases the likelihood of collisional deactivation of $O(^1D)$ due to the high neutral density below ~200 km. This quenching forces the excited atom into a lower energy state before it can radiate. As shown in Figure 1.6, the $O(^1D)$ state lies only 1.96 eV above the ground state; consequently, this emission is easily excited by soft particle precipitation. In addition, thermal excitation by electrons in the high-energy tail of a background Maxwellian distribution can produce $O(^1D)$ atoms. The "classical" production mechanisms, summarized by *Solomon et al.* [1988], are impact excitation by both secondary auroral electrons and thermal electrons, and dissociative recombination of O_2^+:

$$O(^3P) + e \longrightarrow O(^1D) + e \tag{1.7}$$

$$O_2^+ + e \longrightarrow O + O(^1D) \tag{1.8}$$

In addition, *Rees* [1989] presents the atom interchange reaction

$$N(^2D) + O_2 \longrightarrow NO + O(^1D) \tag{1.9}$$

as a major source of $O(^1D)$ atoms. Relaxation to the ground state of the $O(^1D)$ atom is accomplished by:

$$O(^1D) \longrightarrow O(^3P) + h\nu \quad [630.0 \text{ nm}] \tag{1.10}$$

with other loss mechanisms primarily being collisional deactivation [*Solomon et al.*, 1988]:

$$O(^1D) + X(N_2, O_2, e) \longrightarrow O(^3P) + X^* \tag{1.11}$$

with the asterisk implying increased energy.

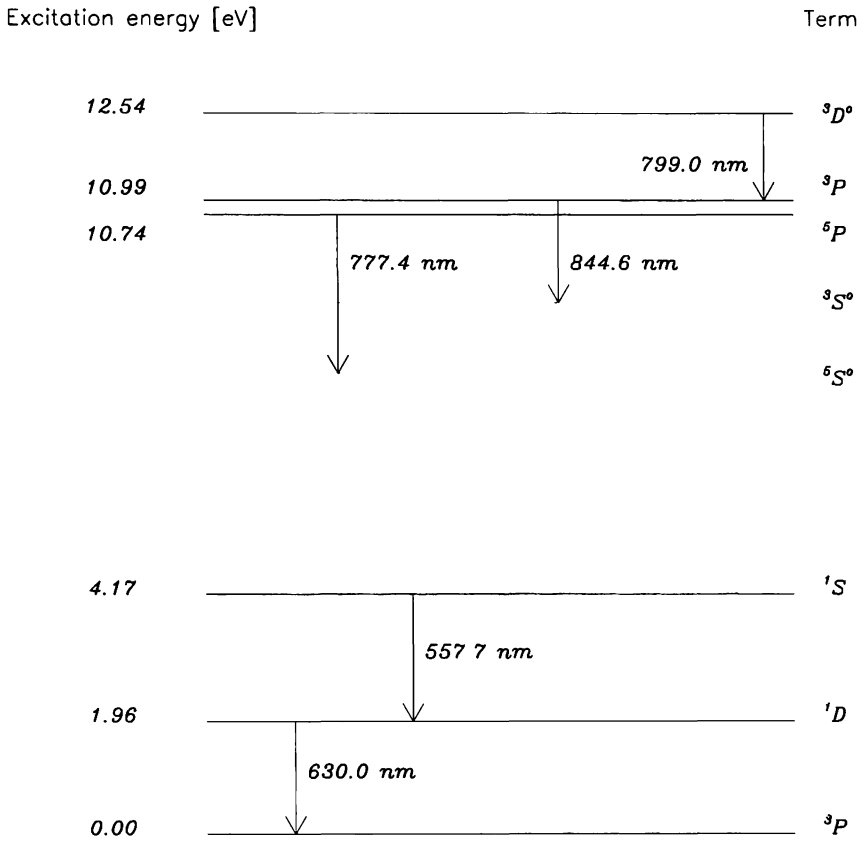

Figure 1.6: A partial energy level diagram of the O atom. Only transitions discussed in the text are identified.

1.2.4 O(^{5}P) 777.4 nm, O(^{3}P) 844.6 nm, and O(^{3}D^o) 799.0 nm emissions

The O(^3P) 844.6 nm and the O(^5P) 777.4 nm are two of the brightest permitted oxygen emissions in the aurora. Both are also observed in the dayglow. These emissions originate from allowed transitions, and have lifetimes on the order of 10^{-6}

to 10^{-7} seconds. Unlike the forbidden red and green lines, these short-lifetime, high-excitation energy emissions are not subject to numerous chemical sources and sinks; they are therefore frequently used to determine atomic oxygen densities. At high altitudes, the O(^5P) and the O(^3P) are formed by direct impact ionization of atomic oxygen

$$O + e \longrightarrow O^* + e \tag{1.12}$$

The ratio of the two emissions' intensities, $I(844.6)/I(777.4)$, is related to the characteristic energy of the precipitating electrons, and can be used as an indicator of auroral heights [*Christensen et al.*, 1978]. For a particular characteristic energy, impact excitation of O for both emissions necessitates $I(844.6)/I(777.4)$ that is constant with altitude; however, the ratio has been observed to decrease at lower altitudes, thus implying a secondary production source for the O(^5P) emission. Laboratory measurements by *Erdman and Zipf* [1987] have shown that dissociation of O_2

$$O_2 + e \longrightarrow O^* + O + e \tag{1.13}$$

produces O(^5P) 777.4 nm, and by utilizing high-resolution (mÅ) spectra, the relative contribution of both production mechanisms can be determined [e.g., *Hecht et al.*, 1985]. Typical auroral intensities for the O(^5P) and the O(^3P) emission are listed in Table 1.2.

The O($^3D^o$) emission is a weak, permitted auroral multiplet at 799.0 nm, formed by electron impact excitation of atomic oxygen. The energy level diagram in Figure 1.6 shows that the 799.0 nm emission leaves an oxygen atom in the (^3P) state, which could then potentially contribute to the 844.6 emission. However, the complicated processes surrounding the 799.0 nm emission's contributions to the 844.6 O(^3P)

and other important atomic oxygen emissions are not completely determined [e.g., *Christensen et al.*, 1983; *Erdman and Zipf*, 1983; *Bahsoun-Hamade et al.*, 1994].

1.2.5 O^+ 732.0–733.0 nm emission

The metastable O^+ 732.0–733.0 nm emission (hereafter, simply referred to as O^+) arises from [*Sivjee et al.*, 1979]:

$$O^+(^2P^o) \longrightarrow O^+(^2D^o) + h\nu \quad [732.0,\ 733.0\ \text{nm}] \tag{1.14}$$

The emission is a blend of multiplets, with prominent doublets near 732.0 and 733.0 nm. Under auroral conditions, the excited ($^2P^o$) and ($^2D^o$) states, together with the (ground) ($^4S^o$) state, are produced by electron impact according to

$$O + e \longrightarrow 2e + O^+(^2P^o,\ ^2D^o,\ ^4S^o) \tag{1.15}$$

with fractions of 0.2, 0.4 and 0.4, and requiring 18.61, 16.92, and 13.61 eV, respectively [*Rees*, 1989]. A partial energy level diagram is shown in Figure 1.7. The emission is also observed in the dayglow, with the excited ($^2P^o$) state formed by direct photoionization of O [*Meriwether et al.*, 1978]:

$$O + h\nu\ (\lambda < 66.7\ \text{nm}) \longrightarrow O^+(^2P^o) + e \tag{1.16}$$

with the lower energy excited states produced similarly.

Below altitudes of ~220 km, quenching by O and N_2 destroys $O^+(^2P^o)$ ions; conversely, above ~270 km, quenching is negligible. Doppler profiles of the emission can be used to derive ion temperatures, assuming sufficient collisions among ($^2P^o$) ions

during their radiative lifetime (5 seconds). High-resolution emission line Doppler shift observations have been made [e.g., *Smith et al.*, 1982]; these ion drift measurements are a tracer of convective patterns in the ionosphere, from which local electric fields can be inferred.

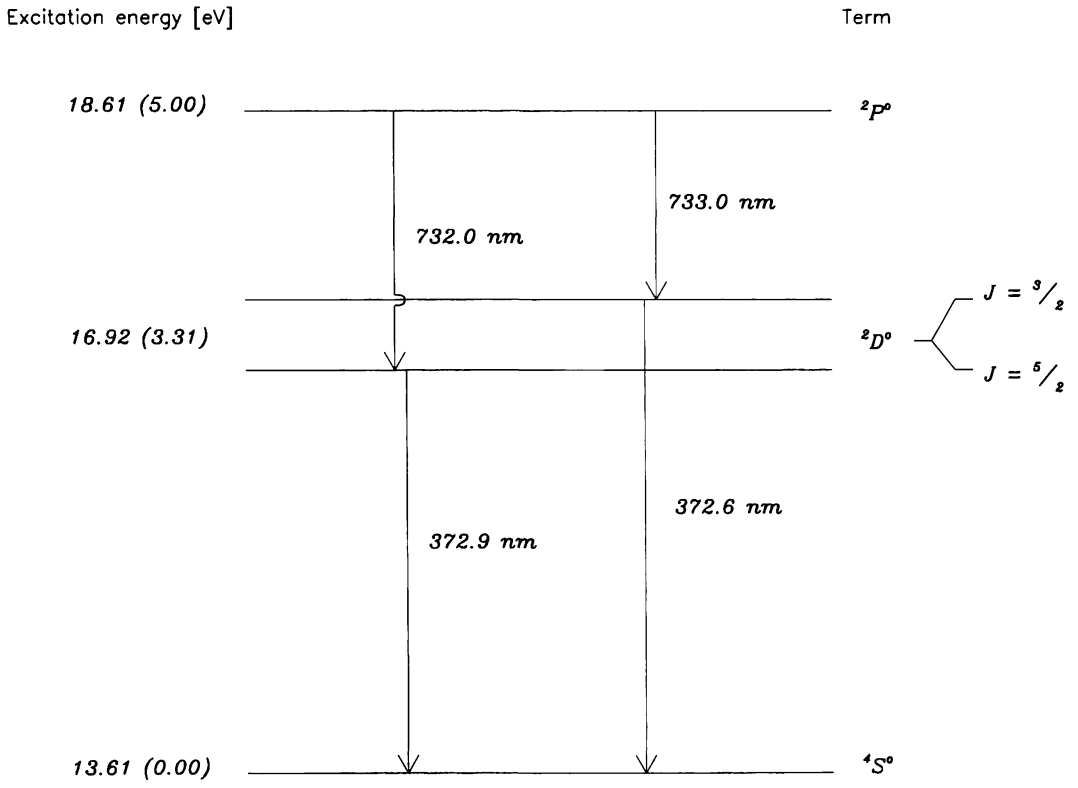

Figure 1.7: A partial energy level diagram of the O^+ ion, showing pertinent transitions. Energy values in parentheses reference the O^+ ground state, which is 13.61 eV above the O ground state.

Having given a brief overview of some important auroral emissions, we will in the following chapter discuss means of artificially stimulating them. Before we do so, however, an introduction to the behavior of radio waves in the ionosphere is required.

1.3 Radio wave propagation in the ionosphere

Radio wave transmission, refraction and reflection are to a large degree determined by the plasma frequency in the propagating media. The index of refraction, n^2, of an electromagnetic wave propagating in the ionosphere (taken to be a cold, magnetized plasma) is given [*Robinson*, 1989] by the Appleton-Hartree formula:

$$n^2 = 1 - \frac{X}{1 - iZ - \frac{\frac{1}{2}Y^2 \sin^2\theta}{1-X-iZ} \pm \frac{1}{1-X-iZ}\left(\frac{1}{4}Y^4 \sin^4\theta + Y^2\cos^2\theta\,(1-X-iZ)^2\right)^{1/2}} \tag{1.17}$$

where

$\omega_h = 2\pi f_h$ = the angular frequency of the heater wave,

$X = \dfrac{\omega_p^2}{\omega_h^2}$ = ratio of the squares of the plasma frequency $\left(\omega_p = \sqrt{\dfrac{n_e e^2}{m_e \epsilon_o}}\right)$ and the heater angular frequency,

$Y = \dfrac{\omega_{ce}}{\omega_h}$ = ratio of the electron cyclotron frequency $\left(\omega_{ce} = \dfrac{B|e|}{m_e}\right)$ to the heater angular frequency,

$Z = \dfrac{\xi}{\omega_h}$ = ratio of the electron collision frequency to the heater angular frequency,

θ is the angle between the local geomagnetic field vector and the direction of propagation of the wave.

Under certain simplifying assumptions, equation 1.17 reduces in complexity. In the F-region ionosphere, $\xi \ll \omega_h$, so collision effects can be ignored ($Z = 0$). With the further restriction $\omega_h > \omega_{ce}$ ($Y < 1$), we can consider two special cases. The first concerns transverse, or perpendicular propagation, where $\theta = \pm\pi/2$. Then equation 1.17 simplifies to:

$$n^2 = 1 - X \tag{1.18a}$$

$$n^2 = 1 - \frac{X(1-X)}{1-X-Y^2} \tag{1.18b}$$

Physically, a wave is reflected when $n^2 = 0$ (a cutoff). The zeros of equations 1.18a and 1.18b enable us to distinguish between two wave modes differing in their polarization and index of refraction. Equation 1.18a gives $X = 1$ for a cutoff; this corresponds to the ordinary, or o-mode wave, which reflects from the altitude where $f_p = f_h$. An ordinary wave reflects from the same altitude whether a magnetic field is present or not, hence the name. The second wave, the extraordinary, or x-mode wave, displays two cutoffs at $X = 1 \pm Y$, and the reflection altitudes are functions of the background magnetic field.

The second special case, longitudinal propagation, occurs when $\theta = 0$. The geomagnetic field and the direction of wave propagation are either parallel or antiparallel. Once again ignoring collisions, the Appleton-Hartree equation reduces to

$$n^2 = 1 - \frac{X}{1 \pm Y} \tag{1.19}$$

Equation 1.19 yields circularly polarized o- and x-mode waves[2] The value $\theta = 0$ is a singular value. Physically significant solutions are obtained for departures from purely longitudinal propagation. Figure 1.8 shows the variation of the index of refraction with altitude for $\theta = 15°$, $Y = 0.5$, $Z = 0$. An x-mode wave launched from the ground reflects from the $1 - Y$ altitude; the o-mode wave reflects from the $X = 1$ altitude, and it generates an x-mode wave close to $X = 1$. For $X > 1 - Y^2$, the right-hand branch of the x-mode wave is sometimes termed the z-mode, and it reflects from the $X = 1+Y$ level. Since this branch of the curve does not extend to $X = 0$ (the bottom

[2]At low latitudes, the waves are linearly polarized. At high latitudes, the o-mode wave is left-hand circularly polarized, such that the rotation of the electric field vector opposes the electron gyromotion. The x-mode is right-hand circularly polarized, in the same sense as the electron gyromotion. For both cases, the thumb points along the ambient magnetic field.

of the ionosphere), the z-mode is not directly detectable from the ground [*Rietveld et al.*, 1993; *Budden*, 1985].

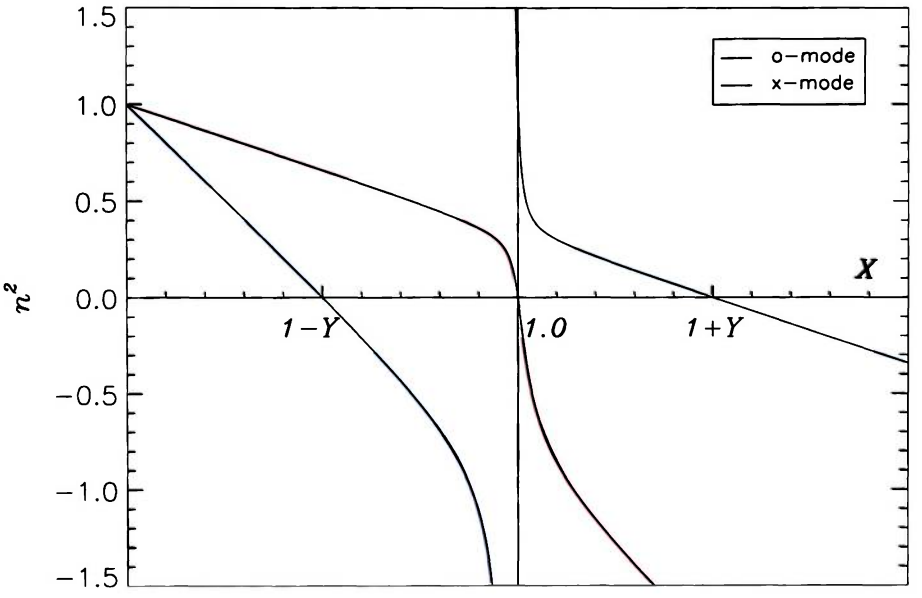

Figure 1.8: Index of refraction as a function of X (ω_p^2/ω_h^2), for small departures from purely longitudinal propagation. The curves were obtained for $Y = \omega_{ce}/\omega_h = 0.5$, $Z = \xi/\omega_h = 0$, and $\theta = 15°$. The parameters are similar to those observed during high-latitude heating experiments.

The different propagation paths and reflection altitudes for the various modes in the northern hemisphere are illustrated in Figure 1.9. Of note is the southward and northward displacement of the waves near reflection. The northward deflection comes about from the requirement that at reflection, the o-mode ray is perpendicular to the Earth's magnetic field [*Budden*, 1985]. The role of the both the southward and northward deflections during ionospheric modification experiments is further explored by *Mjølhus and Flå* [1984] and *Mjølhus* [1990].

Figure 1.9 shows that only o-mode waves within the cone defined by the Spitze

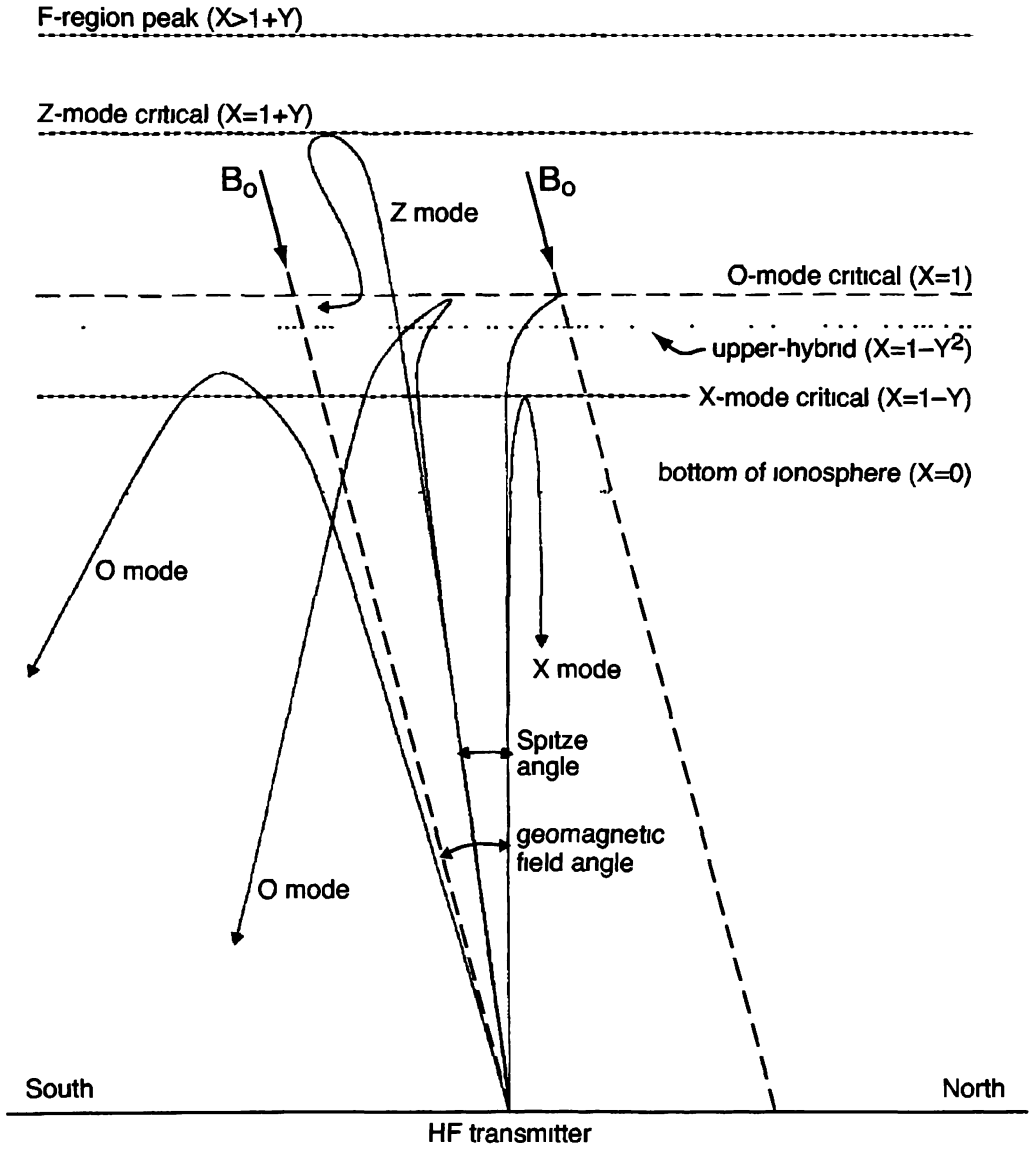

Figure 1.9: Ray paths of different wave polarizations in the northern hemisphere, for small departures from purely longitudinal propagation Critical levels correspond to reflection altitudes The o-mode reflects from a higher altitude than the x-mode Only o-mode waves within the Spitze angle will reach the $X = 1$ altitude (Adapted from *Rietveld et al* [1993])

angle, ϕ_c, will reflect from the $X = 1$ altitude. The Spitze angle is defined as

$$\phi_c = \sin^{-1}\left(\sqrt{\frac{f_{ce}}{f_{ce}+f_h}}\sin\chi\right) \tag{1.20}$$

where χ is the angle between the vertical and the local magnetic field, f_{ce} is the electron cyclotron frequency, and f_h is the heater wave frequency. At high latitudes, $\phi_c \approx 4{-}8°$. The importance of this in ionospheric heating experiments is discussed later.

Some of the exact reflection conditions identified earlier are modified by physical considerations. For instance, due to local fluctuations in the electron density, a radio wave (unless otherwise noted, o-mode is assumed) with frequency f_h, will not reflect from a single altitude, but from a range of altitudes where $f_p \simeq f_h$. In this region, termed the plasma resonance layer (PRL), the wave's group velocity goes to zero, its phase velocity is infinite, and the wave is reflected. Since the plasma frequency is proportional to the electron density, the maximum electron density in the ionosphere, n_{max}, limits the maximum frequency that can be reflected. The relationship between this critical frequency, f_oF_2, and n_{max} is

$$n_{max}\ [\mathrm{m}^{-3}] = 1.24 \times 10^{10}\ (f_oF_2\ [\mathrm{MHz}])^2 \tag{1.21}$$

In the daytime ionosphere, the critical frequency, f_oF_2, is typically 8–9 MHz, corresponding to an $n_{max} \approx 10^{12}$ m^{-3} A radio wave with $f_h > f_oF_2$ will be transmitted through the ionosphere and into space.

Several kilometers below the plasma resonance layer is the upper hybrid resonance layer (UHRL). Similar to the PRL, the UHRL is the region where the upper hybrid

frequency

$$f_{uh} = \sqrt{f_p^2 + f_{ce}^2} \tag{1.22}$$

is equal to the radio wave frequency f_h. The electron cyclotron frequency, f_{ce}, is a function of the local magnetic field strength and thus of altitude.

Figure 1.10 shows various frequency-altitude profiles. The plasma frequency, f_p,

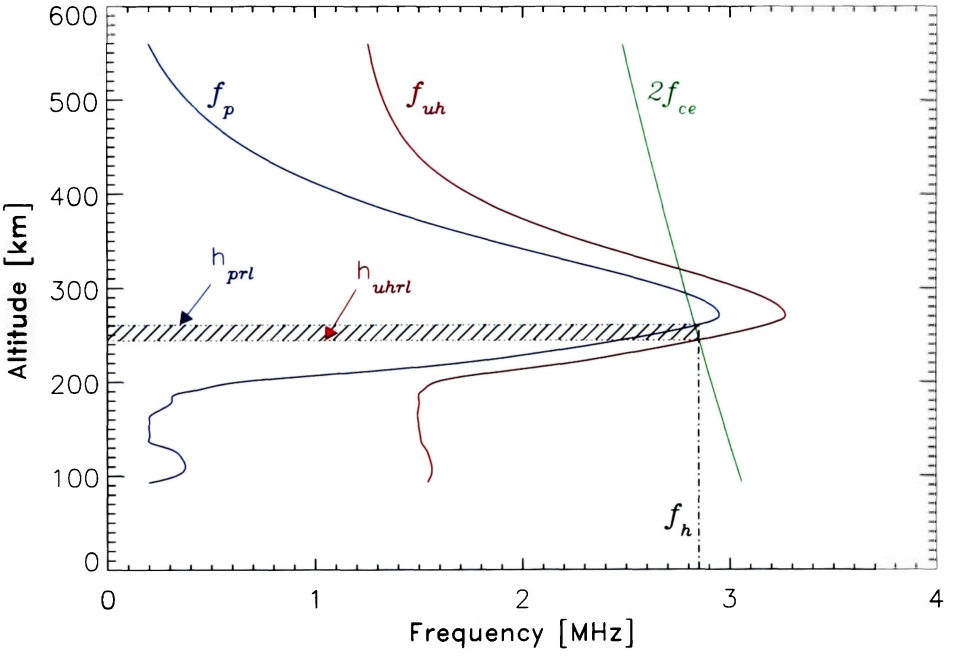

Figure 1.10: Altitude profiles of the plasma frequency, f_p, the upper hybrid frequency, f_{uh}, and $2f_{ce}$, twice the electron cyclotron frequency. Also shown are the plasma resonance layer (h_{prl}), the upper hybrid resonance layer (h_{uhrl}), and the interaction region between the two layers (shaded). A typical heater frequency, $f_h = 2.85$ MHz, is also plotted.

is typically obtained from a Digisonde, and only the lower half of the profile is valid. The electron cyclotron frequency profile is derived from the latest magnetic field model, IGRF10 (http://omniweb.gsfc.nasa.gov/vitmo/igrf_vitmo.html), and is used in conjunction with the plasma frequency profile to obtain f_{uh}, the upper hybrid frequency profile. At a given altitude, the plasma frequency is always less than the

upper hybrid frequency; conversely, for a fixed frequency, the UHRL will always be lower than the PRL.

Between the two layers is the interaction region. During an ionospheric heating experiment, Langmuir waves and upper hybrid waves (discussed in more detail in the following chapter) are generated in the PRL and the UHRL, respectively, and these waves play a dominant role in theories that explain artificial aurora.

Chapter 2

Ionospheric Heating Experiments

Since the mid-1800s, scientists had speculated that a conducting layer existed in the upper atmosphere. In the early 1900s, Marconi used this layer to transmit transatlantic signals. Soon thereafter, commercial radio broadcasting utilizing ionospheric propagation became commonplace. The Luxembourg radio station, in 1933, inadvertently performed the first recorded ionospheric modification experiment; the radio transmitter, one of the most powerful at the time, modulated other radio stations' signals propagating through the same region of the ionosphere [*Bailey and Martyn*, 1934].

Starting in the 1960s and 1970s, scientists began to realize that the ionosphere provides a unique laboratory for the study of wave-plasma interactions. Favorable characteristics of this outdoor laboratory include:

- a wide range of parameter space, with electron density variations of several orders of magnitude, and electron temperature variations of at least one order of magnitude,
- characteristic scale lengths and scale times much longer than many plasma

phenomena, hence experiments are essentially unbounded and long-lived,

- intrinsic magnetic and electric fields, which in auroral regions can be quite large.

Nevertheless, plasma modification attempts, which are some of the few "active" ionospheric experiments, face challenges: they are never conducted in a controlled environment, and the process of diagnosing and interpreting results is often complicated by the same conditions that make these experiments attractive. In addition, the theory of the nonlinear wave-plasma interactions is vast and complex. This has prompted *Walker* [1979] to comment

> "...the history of ionospheric modification by radio waves has been characterized by a failure of theory to predict phenomena before they were observed, combined with a rapid development of theory to accommodate newly observed phenomena. This situation is not surprising. The wealth of possible interactions in a highly nonlinear system is so great that theory depends on observation to guide it into productive paths."

Robinson [1989] lists some wave-plasma interactions that can be studied during ionospheric heating experiments: plasma temperature and density changes, generation of small scale field aligned irregularities, induced anomalous absorption of high frequency (HF) radio waves, artificially induced spread-F, artificially stimulated scintillations, artificially enhanced airglow[1] and particle acceleration, enhanced ion and plasma lines in incoherent radar spectra, nonlinear radio wave reflectivity, stimulated HF emissions, and more. The paper and included references form an excellent overview of ionospheric modification experiments. Because these experiments are

[1]The terms "artificial aurora" and "artificial airglow" are often used synonymously, though the former is preferred.

generally accompanied by a rise in electron temperature (energy), they are often simply termed "heating" experiments.

2.1 Ionospheric heaters

Ionospheric heaters are non-isotropic, HF antennas, with a gain, G_t [dB], in some preferred direction. The effective radiated power (ERP) is thus a product of the antenna gain, G_t, and the input power to the transmitters, P_t. Thus

$$\text{ERP} = P_t \times 10^{G_t/10} \tag{2.1}$$

Since G_t is dependent on the frequency of the radiated wave, the ERP similarly depends on the frequency, with a higher ERP available at higher frequencies. This is an important factor in ionospheric experiments, where the ERP is significant in producing detectable effects. Table 2.1 lists output characteristics of three active heater installations, highlighting the relationship between frequency, gain, ERP, and beamwidth. It bears pointing out that, in general, the large beamwidths produced during ionospheric heating experiments (see Table 2.1) ensure that even for vertical heating, it is possible for a portion of the power to bleed over into the Spitze cone and magnetic zenith.

Ionospheric modification experiments utilizing high frequency radio waves are now in their fourth decade. Significant advances in heater design and diagnostics (especially optics) have provided new and exciting results. In addition to the facilities listed in Table 2.1, *Kosch et al.* [2007b] provide a more comprehensive introduction to heater installations and their capabilities.

From first principles, the electric field, E [V/m], and the energy flux, F [W/m^2],

Table 2.1: Magnetic field orientation and output characteristics for three active heating installations HIPAS has a fixed heater frequency of 2 85 MHz, while EISCAT and HAARP cover the ranges 3 85–8 0 MHz, and 2 8–10 0 MHz, respectively

Facility	χ [°]	Power [MW]	Frequency [MHz]	Gain [dB]	ERP [MW]	Beam width [°]
HIPAS[a]	13	1 2	2 85	18 5	84	22
EISCAT[b]	13	1 2	3 85–5 65	24	300	14 5
			5 5–8 0	24	300	14 5
			5 5–8 0	30	1200	7 5
HAARP[c]	15	3 6	2 8	19 2	300	~18
			10 0	30	3600	~5

[a]High Power Auroral Stimulation, http //www hipas alaska edu
[b]European Incoherent Scatter, http //www eiscat uit no/heater html
[c]High Frequency Active Auroral Research Program, http //www haarp alaska edu

associated with an electromagnetic wave propagating in free space (ignoring absorption and refraction) can be calculated [*Rietveld et al* , 1993] At a distance R [km] from a heater transmitting ERP [kW],

$$E = 0\ 25\sqrt{(ERP)}/R \qquad F = 7\ 96 \times 10^{-5}\ (ERP)/R^2 \qquad (2\ 2)$$

These quantities are calculated in Table 2 2 at an F-region interaction altitude of 250 km The field strength E is generally reduced by absorption and refraction but under some conditions, e g , at high latitudes, it can increase by over an order of magnitude due to a process called swelling [*Lundborg and Thidé*, 1986] How does the radio wave energy flux compare to values encountered during natural processes in the ionosphere?

Wygant et al [2000] states that the weakest ionospheric electron energy fluxes capable of producing visible emissions in natural aurora are ~1 mW/m^2, but values as

Table 2.2: The electric field and energy flux associated with a pump wave, at an interaction altitude of 250 km. These quantities are calculated for the low frequency ranges.

Facility	Frequency [MHz]	ERP [MW]	E [V/m]	F [mW/m^2]
HIPAS	2.85	84	0.29	0.1
EISCAT	3.85-5.65	300	0.55	0.38
HAARP	2.8	300	0.55	0.38

high as 500 mW/m^2 have been observed. Typical values are ~20 mW/m^2 Given that electrons are not necessarily the largest source of energy deposition during auroras, it is clear that energy fluxes produced during ionospheric heating are smaller than those occurring during natural auroral processes. Even the largest heater fluxes currently producible (~5 mW/m^2), are minuscule compared to the solar constant at ionospheric altitudes (~1350 W/m^2), which is six orders of magnitude larger. Furthermore, the highly dynamic nature of the ionosphere ensures that once a heating pulse is turned off, localized enhancements in electron temperatures are "swept clean" in a time frame of minutes [e.g., *Gustavsson et al.*, 2006].

During a heating experiment, several key parameters need to be selected. Of prime importance is the frequency, since most phenomena (including our focus, the production of artificial aurora), are sensitive to multiples of the gyrofrequency, f_{ce}. The selected frequency also constrains the ERP. An experimenter has a choice of polarizations to employ, though x-mode heating at high latitudes generally produces no observable optical effects [e.g., *Kosch et al.*, 2003]. The magnetic dip angle χ plays an important role in determining propagation characteristics and wave-plasma interactions, so the beam pointing direction has to be carefully selected. Beam-steering by several degrees is possible in the N-S plane; some heaters have E-W

capabilities too. The transmitted waveform can be frequency or amplitude modulated.

Artificial aurora production mechanisms are fast-acting (order of seconds or less), and most heaters can produce pulsed, millisecond-varying signals. However, because some excited states have relatively long lifetimes, and to enable detection by optical instruments, continuous wave (CW) heater duty cycles ranging from 1−5 minutes on/off are employed. A common heating mode for the generation of artificial aurora is full power, 2.85 MHz ($2f_{ce}$); at a duty cycle of 2 minutes on, 2 minutes off; CW, o-mode, and "up-**B**" (antiparallel to the magnetic field in the northern hemisphere).

Environmental conditions play a large role in the success of artificial aurora experiments, and these are beyond the control of the experimenter. Optimal conditions include cloud-free and dark skies, low geomagnetic activity, no natural aurora, and sufficient plasma density ($f_oF_2 \geq f_h$). Additionally, radio wave absorption—energy losses from electrons colliding with neutrals, ions or other electrons, due to high ionization in the D region—should be negligible.

The two main heating facilities in the world, HAARP and EISCAT, possess an extensive set of diagnostic equipment. Both have nearby SuperDARN (Super Dual Auroral Network) HF radars that observe backscatter produced or enhanced by plasma irregularities. HAARP and EISCAT also have UHF incoherent scatter radars (ISRs) that, through plasma and ion line measurements, are able to infer Langmuir and ion acoustic waves, respectively. Only the EISCAT ISR, however, is sensitive enough to measure electron and ion temperature enhancements, although a planned upgrade to the HAARP ISR will allow similar measurements. Digisondes (to obtain ionospheric plasma parameters) and riometers (to measure radio wave absorption) are standard at most installations, as is dedicated optical instrumentation.

2.2 Artificial aurora production mechanisms

During a heating experiment designed to produce optical emissions, a wave with frequency $f_h \lesssim f_o F_2$ is usually transmitted vertically or up-**B**. Wave-particle interactions fuel mechanisms that accelerate electrons; these electrons excite neutral (or ionized) constituents of the F-region plasma, leading to the production of artificial aurora. Thus, the essential difference between natural and artificial aurora is the mechanism responsible for the accelerated electrons. For o-mode heating, three main wave-particle interactions produce artificial aurora. For all the methods, meter-scale, field-aligned plasma density depletions, also known as striations, play an important role. Figure 2.1 illustrates a basic heating experiment.

Airglow production methods are delineated by the "plasma resonance" and "double resonance" conditions. At plasma resonance, $f_p = nf_{ce} = f_h$, that is, the plasma frequency matches the n^{th} gyroharmonic, at the height where they are both equal to the heater frequency. Similarly, double resonance is satisfied when $f_{uh} = nf_{ce} = f_h$. This is illustrated in Figure 2.2 for $n = 2$. At frequencies close to the resonance conditions, efficient acceleration of electrons leads to significant increases in radio-induced optical emission (RIOE) intensity. Next we summarize the main artificial aurora production methods discussed in detail by *Mishin et al.* [2005] and *Kosch et al.* [2007a].

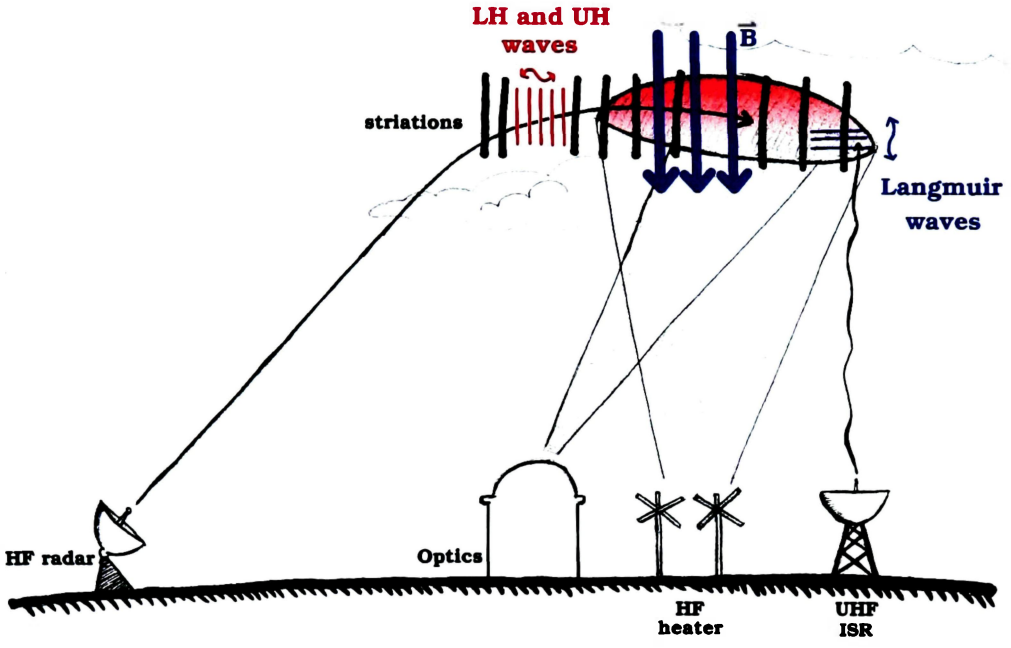

Figure 2.1: A typical artificial aurora experiment: wave-plasma interactions accelerate electrons in a heated volume (~250 km altitude, shaded red), stimulating auroral emissions detected by optical instrumentation. Naturally occurring, meter-scale striations (density irregularities) grow during heating, enhancing backscatter observable by HF radars. Mode conversions and wave interactions generate, among others, (i) Langmuir waves propagating parallel to **B**, and (ii) lower hybrid (LH) and upper hybrid (UH) waves propagating perpendicular to **B**. Ground based radars detect the effects of these waves. For simplicity, the magnetic field is vertical.

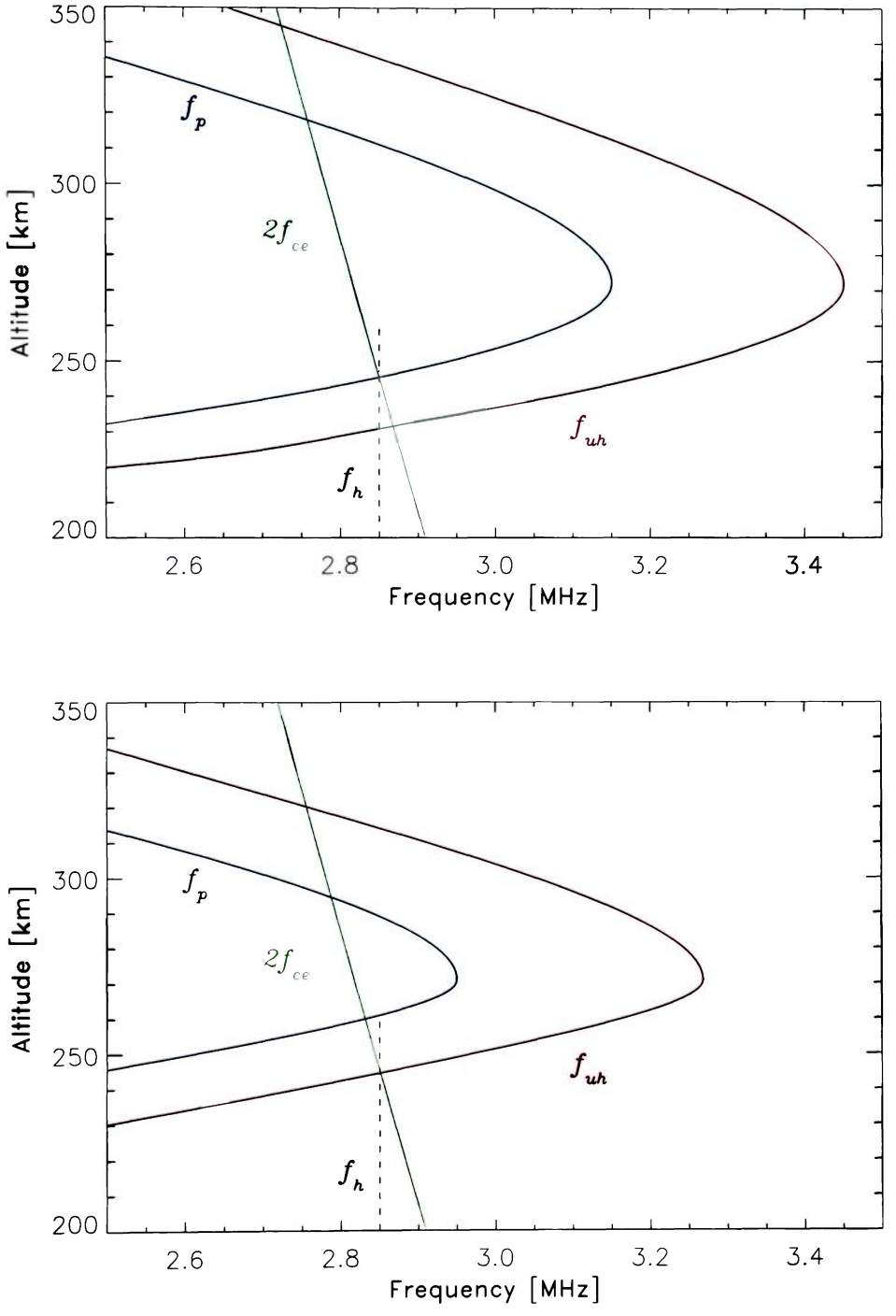

Figure 2.2: Profiles of the plasma frequency (f_p), upper hybrid frequency (f_{uh}), twice the electron cyclotron frequency ($2f_{ce}$), and the heater frequency (f_h), illustrating plasma resonance (top), when $f_p = 2f_{ce} = f_h$, and double resonance (bottom), when $f_{uh} = 2f_{ce} = f_h$. The profiles were obtained at dusk, with the resonance conditions separated by ~30 minutes.

1. Langmuir wave parametric decay instability and oscillating two-stream instability ($\mathbf{PDI}_L$)

A parametric decay instability is simply the conversion of the pump wave into two or more lower frequency waves, while conserving energy and momentum [*Swanson*, 2003]. Thus, PDI_L is the decay of the electromagnetic o-mode heater wave into a Langmuir (L) and an ion acoustic (IA) wave. Symbolically, EM $\rightarrow$ L + IA. On the other hand, the oscillating two-stream instability (OTSI) occurs when a plasma is uniformly driven by a pump wave, with the production of secondary waves and density cavities (cavitons). Thus, OTSI_L is EM $\rightarrow$ L + δn_e. At high latitudes, PDI_L produces electrostatic Langmuir (plasma) and ion acoustic waves that propagate near-parallel to the magnetic field. By pointing up the field line, UHF incoherent scatter radars can detect plasma line and ion line backscatter enhancements caused by the waves. For up-**B** pumping at angles larger than the Spitze cone, the large difference between f_h and f_p at the reflection altitude precludes the development of OTSI_L. Nevertheless, PDI_L is still possible; because, as shown by *Mishin et al.* [2001], part of the pump wave electric field is parallel to the magnetic field in the region of downward reflection. *Kosch et al.* [2007a] calculated that PDI_L is possible for up-**B** heating as long as $\chi < 17°$.

2. Electron Bernstein and upper hybrid wave parametric decay instability ($\mathbf{PDI}_{EB/UH}$)

Istomin and Leyser [1995] showed that the parametric decay of the electromagnetic o-mode pump wave can produce electrostatic upper hybrid (UH) and electron Bernstein (EB) waves, coupled to lower hybrid (LH) waves, that is, EM $\rightarrow$ UH/EB + LH. The frequency regime and plasma dispersion characteristics determine whether

UH or EB waves are generated. For $2f_{ce}$, EB and UH waves exist below and above the gyroharmonic, respectively, with PDI_{EB} occurring close to the resonance condition. LH waves are trapped in plasma cavitons, and oscillate perpendicular to the magnetic field. Collapse of the cavitons accelerates electrons along magnetic field lines, leading to the generation of artificial aurora. Striation growth associated with UH waves, and LH cavitons both enhance radar backscatter, which, assuming favorable propagation conditions, will be detected by side-looking HF radars. Effects accompanying $\mathrm{PDI}_{EB/UH}$ are observed in < 10 ms.

3. Upper hybrid wave thermal parametric instability ($\mathbf{TPI}_{UH}$)

The third main o-mode wave interaction is a thermal parametric instability [*Grach et al.*, 1981], in which the pump wave is converted into UH waves in the naturally-occurring plasma density irregularities. A positive feedback ensues, whereby the UH waves are trapped in the striations; this causes heating, which leads to ejection of plasma, and consequently, further density depletion and trapping. Striation growth due to UH waves occurs in seconds. TPI_{UH} is easily stimulated, and is present after double resonance when heating at $2f_{ce}$.

Kosch et al. [2007a] have presented data suggesting that all three mechanisms were simultaneously in operation, while *Mishin et al.* [2005] have shown TPI_{UH} and PDI_{UH} co-existing, with equal contributions to RIOE intensity. Figure 2.3 provides a summary of these mechanisms: for pumping in the magnetic zenith on $2f_{ce}$, in an overdense, decaying ionosphere, PDI_{L} and PDI_{EB} are possible before plasma resonance (1) and until double resonance (2). PDI_{UH} takes over from PDI_{EB} at double resonance, with TPI_{UH} starting and PDI_{L} continuing. Nevertheless, PDI_{L} lasts only seconds into the heater-on period; striations (from TPI_{UH}) in the UHRL absorb the pump wave, and prevent it from reaching the $f_p = f_h$ matching altitude. Once the

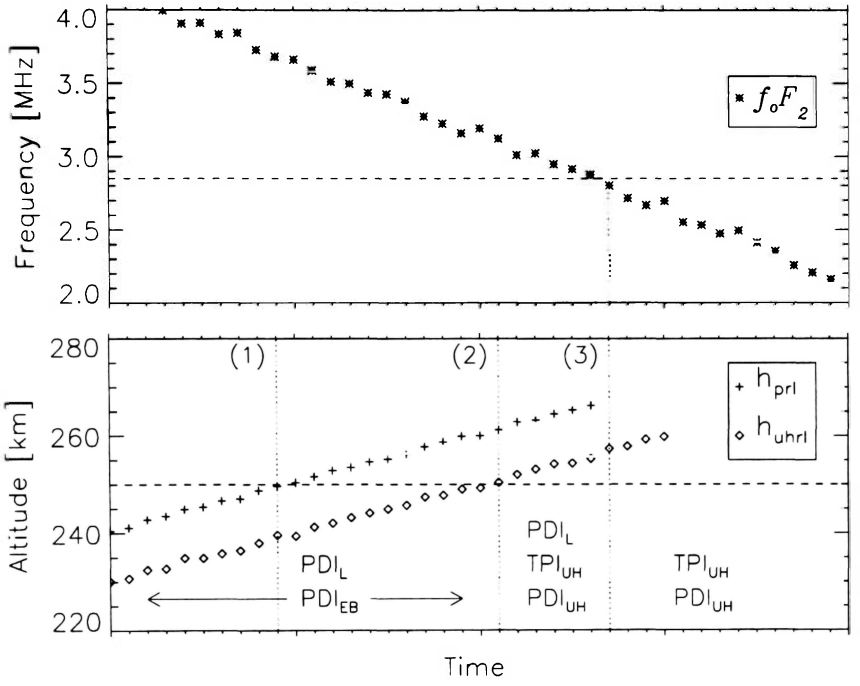

Figure 2.3: Frequency regimes of the different artificial aurora mechanisms, in a decaying ionosphere (dusk). The top panel shows the ionospheric critical frequency, f_oF_2. In the lower panel, the heights of the PRL and the UHRL are plotted. Vertical lines (1), (2), and (3) represent plasma resonance, double resonance, and the transition to an underdense ionosphere, respectively. The timing of the mechanisms is discussed in the text.

ionosphere turns underdense (3), TPI_{UH} and PDI_{UH} continue until the maximum upper hybrid frequency exceeds the ionospheric critical frequency, $f_{uh,max} > f_oF_2$. Artificially induced optical emissions generally cease then.

2.3 Historical overview

Early radio-induced optical emission (RIOE) observations were first made at the Platteville heater in Colorado in the early 1970s. These experiments featured < 100

MW ERP, long (~10 min) heater on/off cycles, frequencies just below f_oF_2, and low-sensitivity optics. Consequently, the majority of observations were of the bright and easily-stimulated $O(^1D)$ 630.0 nm emission. However, one early detection of RIOEs [*Evans et al.*, 1970] is the $O_2(^1\Delta_g)$ band at 1270 nm, presented in Figure 2.4. This notable exception shows enhancements of 5−10% and was produced at an ERP of 50 MW. Previous attempts by the authors to detect any emissions, using photometers focused directly on the heated volume, had failed: the accelerated electrons moved down the field lines and produced the airglow outside the instrument's narrow field of view.

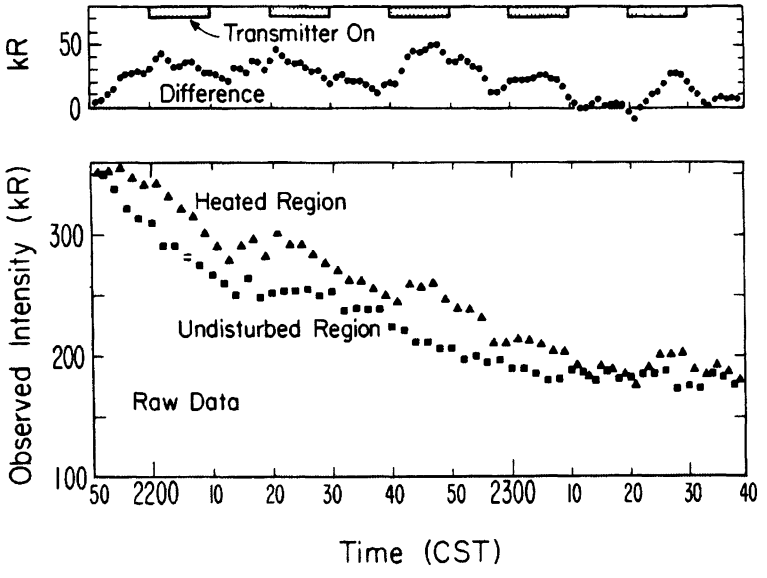

Figure 2.4: An early detection of radio-induced $O_2(^1\Delta_g)$ (1270 nm), by *Evans et al.* [1970].

From the same facility, *Biondi et al.* [1970] utilized $O(^1D)$ observations to determine electron temperature (T_e) enhancements of 30% by monitoring the effect of increased T_e on the rate of $O(^1D)$ production (equation 1.8). Later experiments at

Platteville [e.g., *Sipler and Biondi*, 1972; *Haslett and Megill*, 1974] with an upgraded transmitter led to significantly brighter O(^1D) enhancements (250 R). The latter also detected heater-modulated O(^1S) and correctly surmised that the electron distribution function required to generate these emissions had to be non-Maxwellian.

At lower latitudes, *Gordon and Carlson, Jr* [1974] and *Sipler et al.* [1974] conducted experiments at the Arecibo heating facility, and detected enhancements and suppressions in O(^1D) intensity while heating in o-mode and x-mode, respectively. This was in accord with earlier work performed at Platteville. An overview of early HF heating experiments at low latitudes is provided by *Carlson and Duncan* [1977].

In the late 1970s, a third heater near Moscow [*Adeishvili et al.*, 1978] entered service and produced up to 30 R of O(^1D) while pumping on $1f_{ce}$. *Bernhardt et al.* [2000] conducted heating experiments at another mid-latitude installation, SURA, and was able to estimate, among other quantities, the electric fields (governed by $\mathbf{E} \times \mathbf{B}$ drifts), neutral winds, diffusion coefficients, and collisional quenching times, determined from the growth and decay of the airglow clouds.

The difference in magnetic field configuration at low and high latitudes produces contrasting results during heating experiments. Unfortunately, since the late 1990s, ionospheric heating has primarily been carried out at high latitudes, with no equatorial heaters currently in operation. Northern sites have produced exciting, unpredictable, and sometimes unexplainable results. *Kosch et al.* [2007b] present salient developments pertaining to high-latitude observations of RIOEs. Next we highlight and expound on their work.

From an experiment on 5 October 1981, *Stubbe et al.* [1982] reported the first detection of RIOEs at a high latitude facility, EISCAT. A 5.423 MHz, 260 MW o-mode heater wave produced unusual photometer observations: ~50% increases in red line intensity, accompanied by ~15% decreases in green line intensity. Earlier

o-mode heating at lower latitudes generally enhanced both the red and green line. As discussed later, this is also the case for high latitude heating. Contradicting the results of *Stubbe et al.* [1982], *Henriksen et al.* [1984], from the same experiment, reported no heater-attributable red or green line modulation. The latter used a suite of four remote and co-located meridian-scanning photometers and spectrophotometers.

Although they did not directly detect any heater-induced optical variations, *Sergienko et al.* [1997] reported artificially modulating a natural aurora. A frequency analysis of the auroral pulsations weakly matched the heater modulation frequency of 0.5 Hz. A 270 MW, 4.544 MHz, x-mode pump beam was used.

Brändström et al. [1999] presented the first unambiguous detection of artificial auroral emissions at high latitudes (EISCAT). In an experiment performed on 16 February 1999, they utilized a 4.04 MHz o-mode wave, 210 MW ERP, 4 min on/off cycle, and were pumping 6° from vertical. RIOEs were detected by six remote CCD-equipped imagers. Their O(^1D) data, displayed in Figure 2.5, was estimated to be 300 $\pm$ 100 R. *Gustavsson et al.* [2001] tomographically inverted this data to obtain the first estimates of the heater-induced O(^1D) volume emission rate. They also showed that several heating pulses exhibited two separate excitation regions before growing and merging. Additionally, a comparison of their observations and model results indicated a non-thermal heater-accelerated electron energy spectrum.

Soon after the success of *Brändström et al.* [1999], *Kosch et al.* [2000] (EISCAT) and *Pedersen and Carlson* [2001] (HAARP), in quick succession, observed radio-induced red line emissions. Both noted that the brightest optical emissions sometimes occurred outside the beam -3 dB (half power) limits, despite the electric field and energy flux being greatest in the center of the beam. Also of interest was the fact that the emitting region was displaced toward the magnetic zenith, even for vertical heating. *Gurevich et al.* [2001], working with these observations, theorized that self-

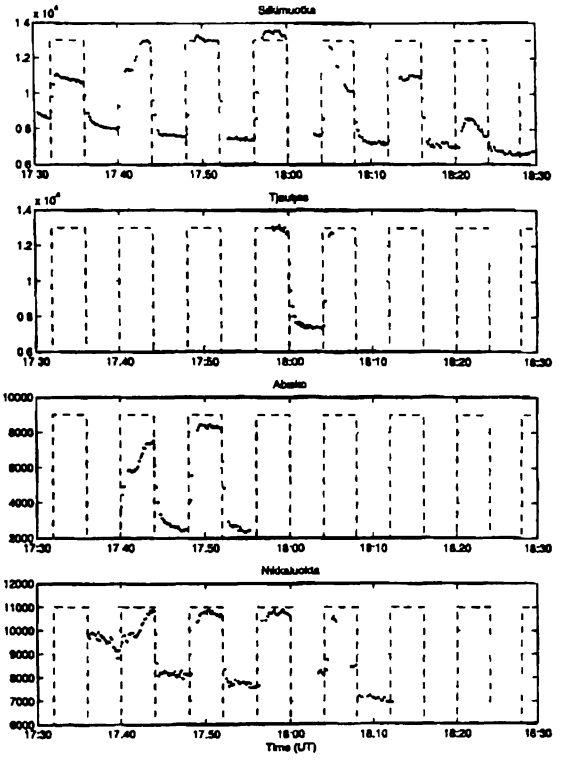

Figure 2.5: O(^1D) emissions from an early high-latitude experiment, observed from multiple remote locations by *Brandstrom et al* [1999] The square wave corresponds to the heater pump cycle The emission intensity was estimated to be 300 ± 100 R

focusing of the pump wave by striations could form a region of accelerated electrons that was aligned in the magnetic field direction

Beam-swinging experiments by *Kosch et al* [2003] and *Pedersen et al* [2003] confirmed that the intensity of RIOEs at high latitudes was almost always in the magnetic zenith direction By stepping the pump beam in multiple azimuth and elevation angles, they concluded that the optical emissions were preferentially generated up-**B**, with gains exceeding one order of magnitude over other directions Nevertheless, interesting and still unexplained results from a beam-swinging experiment were presented by *Kosch et al* [2004]

> "...the pump beam zenith angle was moved in 3° steps along the north-south meridian from 3°N to 15°S, with one pump cycle per position. Only when pumping in the 9°S position were annular optical structures produced quite unexpectedly. The annuli were approximately centered on the pump beam but outside the −3 dB locus. The optical signature appears to form a cylinder, which was magnetic field-aligned, rising above the pump wave reflection altitude. The annulus always collapsed into the well-known optical blobs after ~60 s, whilst descending many km in altitude. All other pump beam directions produced optical blobs only."

Figure 2.6 shows their calibrated red line measurements. The ring-shaped structure at pump-on (top), straddling the −3 dB edge of the beam, and the blob formed close to pump-off (bottom), are shown. Produced at $\sim 4f_{ce}$, with 550 MW ERP, these results have not been duplicated. There is no satisfactory explanation why the structures formed at one position (9° S) only.

Theory predicts [e.g., *Mjølhus*, 1993], and radar backscatter confirms [e.g., *Honary et al.*, 1999] that the growth of striations is suppressed for nf_{ce}, $n \geq 3$. Striations are symbiotic with upper hybrid waves, which are intimately associated with many heating-induced phenomena [e.g., *Hughes et al.*, 2003, 2004], and with the production of RIOEs via the PDI_{UH} and TPI_{UH} mechanisms [*Kosch et al.*, 2002]. Suppressed striation growth implies a decrease in optical emission production for $n \geq 3$. Data for $n = 3$ [*Kosch et al.*, 2002], and $n = 4$ [*Gustavsson et al.*, 2006] confirms this. The exact opposite is true, however, for $2f_{ce}$: (i) there is no minima in striations or emission intensity, and (ii) photon production is an order of magnitude greater than for any other pump frequency [*Kosch et al.*, 2005].

An asymmetry exists in RIOE production about nf_{ce}, $n = 2, 3, 4$, with greater

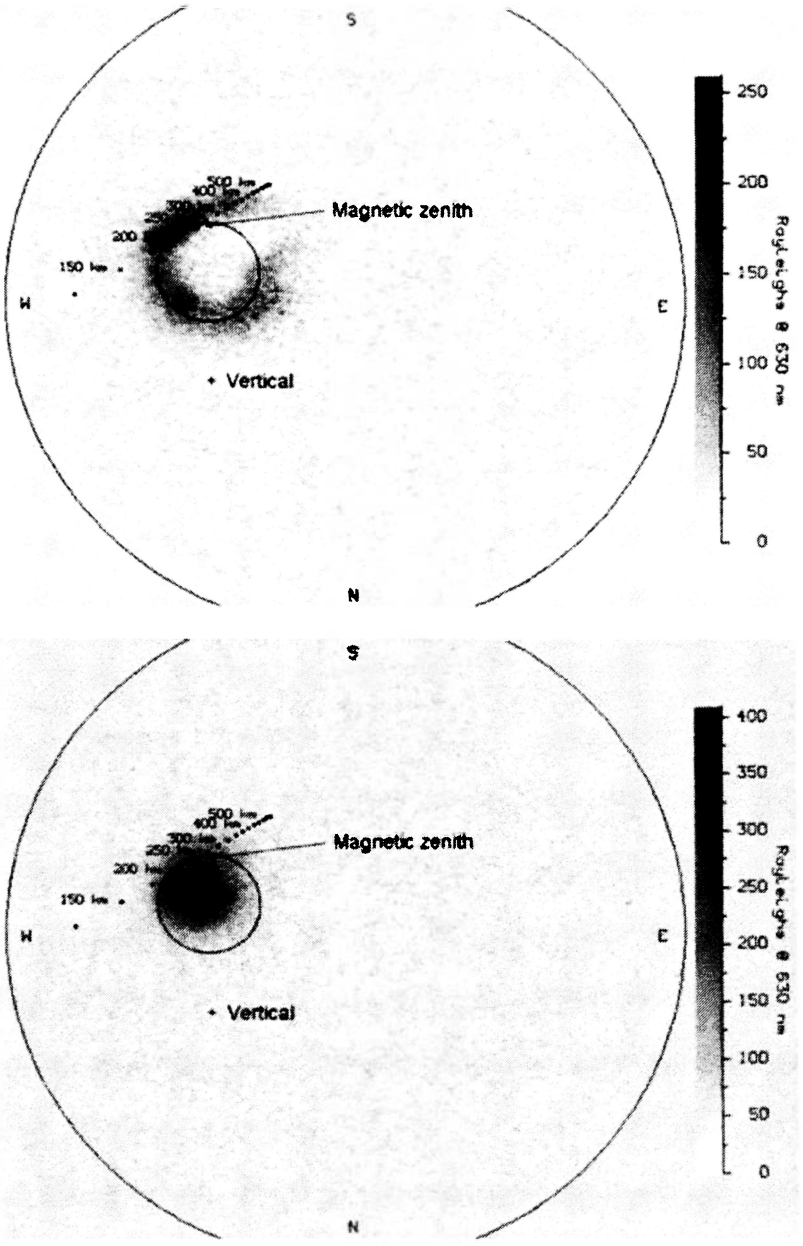

Figure 2.6: Unusual optical structures observed by *Kosch et al.* [2004] during a beam-swinging experiment. The start (top) and end (bottom) of the heater pulse, showing annular O(^1D) structures straddling the −3 dB locus, and later collapsing into a blob. The magnetic field line, magnetic zenith, and vertical directions are shown.

emission production above a gyroharmonic than below. *Istomin and Leyser* [2003], among others, predicted this asymmetry for $n \geq 3$. Later, *Kosch et al.* [2005], using $O(^1D)$ and $O(^1S)$ data, provided evidence for this effect for $n = 2$. *Gustavsson et al.* [2006] observed the asymmetry in N_2^+ (427.8 nm) data for $3f_{ce}$ and $4f_{ce}$, but not in simultaneous $O(^1D)$ data. Nevertheless, this asymmetry seems to be a standard occurrence, at least for $n = 2$ (see, e.g., *Kosch et al.* [2007a]).

We now turn our attention to optical emissions that have been detected during F-region heating experiments. For decades, observations of RIOEs were almost exclusively limited to the forbidden $O(^1D)$ 630.0 nm and $O(^1S)$ 557.7 nm excited states. The $O(^1D)$ red line is frequently detected, since it is not strongly quenched in the F region, and has a relatively low excitation energy of 1.96 eV. Similarly, the $O(^1S)$ green line, with an excitation energy of 4.17 eV, is also observed in most experiments, albeit with lower intensities. However, the effective excitation thresholds of the $O(^1D)$ and $O(^1S)$ states are raised to ~3.1 and ~5.4 eV, respectively, due to absorption of 2.0–3.5 eV electrons by N_2 vibrational states [*Bernhardt et al.*, 1989].

In some of the first results from $2f_{ce}$ pumping, *Djuth et al.* [2005] reported small (< 10 R) enhancements of $O(^5P)$ 777.4 nm. The results were obtained for o-mode, up-**B** heating at HAARP with 10 MW ERP. The relatively high excitation energy of 10.74 eV attests to a non-Maxwellian distribution of heater-induced electron energies. Soon thereafter, *Gustavsson et al.* [2005] documented $O(^3P)$ 844.6 nm (10.99 eV) emissions of ~15 R. They used multiple wavelength optical data ($O(^1D)$ 630.0, $O(^1S)$ 557.7, $O(^3P)$ 844.6, and N_2^+ 427.8 nm), electron densities, electron temperatures, and ion temperatures to produce an estimate of the pump-enhanced electron energy distribution (Figure 2.7).

Several features of the distribution function are worth noting. The low energy distribution is Maxwellian-like and exhibits a bite-out at 2 eV, due to absorption by

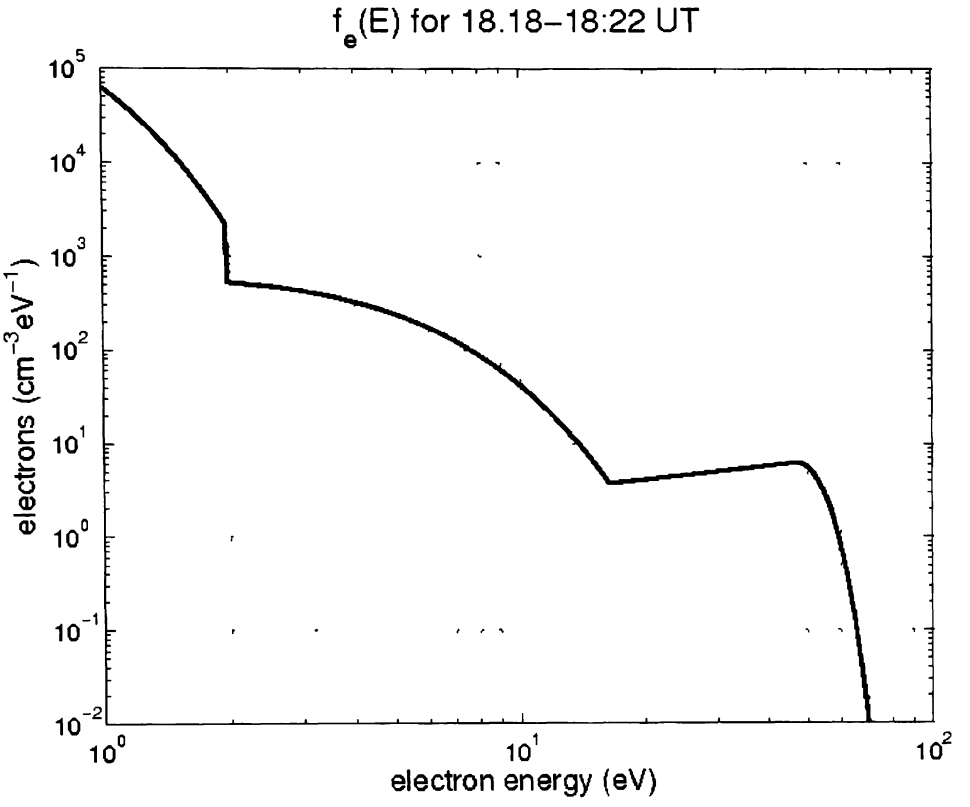

Figure 2.7: An estimate of the pump-enhanced electron energy spectrum generated during HF heating of the ionosphere (From *Gustavsson et al.* [2005].)

N_2 vibrational states. Between 15–45 eV the accelerated component is essentially flat. Finally, there is a small but significant suprathermal distribution of energies in the high-energy tail, caused by Langmuir waves accelerating electrons. The existence of a non-thermal tail seems to have acquired "universal acceptance" [*Bernhardt et al.*, 1989] and is responsible for the high $O(^1S)$ / $O(^1D)$ ratios observed during heating experiments.

The first unambiguous reports of heater-induced ionization were presented by *Holma et al.* [2006] and *Gustavsson et al.* [2006] Both observed N_2^+ 427.8 nm, which has an excitation energy of 18 75 eV above the ground state. *Holma et al.* [2006] were

heating with a 550 MW, 5.425 MHz, 2 min on/off duty cycle, while *Gustavsson et al.* [2006] utilized an o-mode, 2 min on/1 min off, power-ramping mode, with maximum ERPs of 490 and 586 MW. The large radiated powers, and by association the large electric fields and energy fluxes, were probably significant in producing this higher-energy emission; however, heater ERP is only one of many factors involved in the generation of RIOEs. For example, *Pedersen et al.* [2003] found that O(^1S) intensity appeared to positively correlate with heater ERP, whereas O(^1D) intensity eventually saturated, even for higher ERPs. In addition, an analysis of over 1,000 images showed that O(^1D) emissions were stimulated at ERPs as low as ~2 MW, and that red line intensity was largely independent of transmitter frequency.

Mutiso et al. [2008] have recently made two new additions to the list of known RIOEs: the O^+ 732−733.0 nm and O($^3D^o$) 799.0 nm emissions. These are further discussed in Chapter 4. In addition, observations (by the author) from the recent HAARP 2008 Optics Campaign indicate the first detection of radio-induced O_2 Atm (1,1) enhancements. All three emissions were detected using a grating spectrometer, described in the following chapter. In the forty years of ionospheric heating, the overwhelming majority of optical observations have been carried out using photometers and all-sky imagers. The high throughput and temporal resolution of these instruments, coupled to the fact that experimenters were mostly focused on the easily stimulated red and green lines, made these instruments a suitable choice. However, the growing interest in determining the spectrum of a heated volume necessitates a spectrometer sensitive enough to detect weaker RIOEs within a reasonable exposure time. The obvious tradeoff is a loss of throughput resulting in reduced temporal resolution.

To conclude this chapter, we mention the only heating experiment that has produced visible enhancements. While performing E-region heating during a natural

Table 2.3: A list of observed radio-induced optical emissions, and their excitation energies above the ground state.

Emission	Wavelength [nm]	Excitation energy [eV]
$O(^1D)$	630.0	1.96
$O(^1S)$	557.7	4.17
$O(^5P)$	777.4	10.74
$O(^3P)$	844.6	10.99
$O_2(^1\Delta_g)$	1270	0.98
O_2 Atm (1,1)	768.4	1.61
$O(^3D^o)$	799.0	12.49
O^+	732.0	18.61
N_2^+	427.8	18.75

aurora, *Pedersen and Gerken* [2005] produced 4 kR $O(^1S)$ 557.7 nm "speckles" that were $\sim 1^\circ$ in size and positively correlated to the heater. This intensity exceeds the detection threshold of the eye, which is about 1 kR at 550 nm [*Sandholt et al.*, 2002]. All other observed RIOEs have been sub-visual, with intensities ranging from tens to hundreds of Rayleighs. Sadly, the experimenters failed to witness this historic moment, as they were indoors tending their instrumentation.

Chapter 3

Instrumentation, Experiment Description, and Data Analysis

"Welcome to the SPRL Dome of Pain. Get ready for some heavy weightlifting."
Lisandro Martinez

3.1 The HIPAS heating facility

The High Power Auroral Stimulation (HIPAS) Observatory, located in Two Rivers, Alaska (64.9° N, 146.8° W) operates a suite of instruments used in the study of the high-latitude ionosphere. The primary instrument is the HF ionospheric heater. The heater consists of 8 crossed-dipole antennas capable of transmitting up to 70 MW ERP at a frequency of 2.85 MHz. This pump frequency is approximately equal to the local 2$^{\text{nd}}$ electron gyroharmonic ($2f_{ce}$) at F-region heights. The nominal beam width is 22°, corresponding to an area roughly 50 km $\times$ 50 km at an interaction altitude of 250 km. The heater can perform 100 Hz$-$20 kHz amplitude modulation and 0$-$20 kHz phase modulation. Currently, HIPAS is only one of two heaters worldwide capable

of transmitting at $2f_{ce}$. This is important because the optical response to heating at frequencies close to $2f_{ce}$ is distinctly different from that at higher gyroharmonics.

3.2 The CCD spectrometer

Optical spectra were obtained using a 0.5-m, $f/4.5$, modified Czerny-Turner grating spectrometer, utilizing a CCD camera controlled by a personal computer. The instrument is depicted in Figure 3.1.

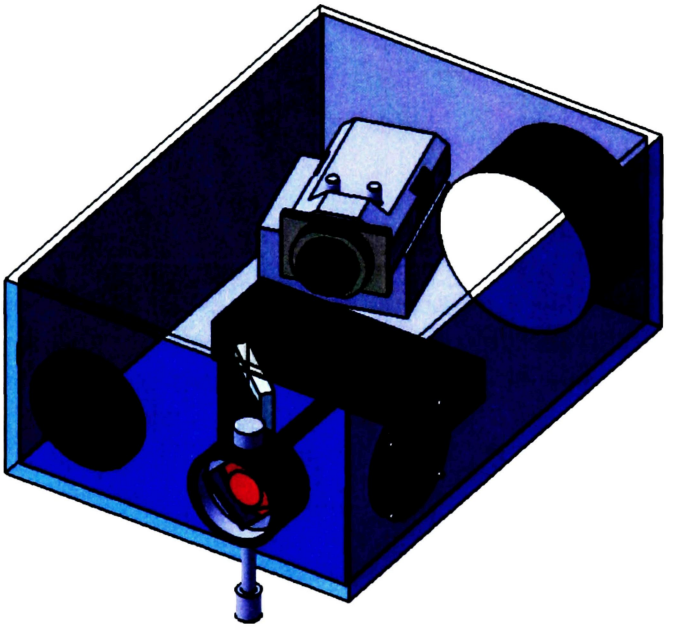

Figure 3.1: A model showing the main components of the 0.5-m spectrometer.

Due to the extremely weak (< 5 R) emissions, the spectrometer was optimized for low-level light detection. The throughput was enhanced by a long entrance slit, and large, high-reflectivity optics. Figure 3.2 shows the layout of the principal optical elements.

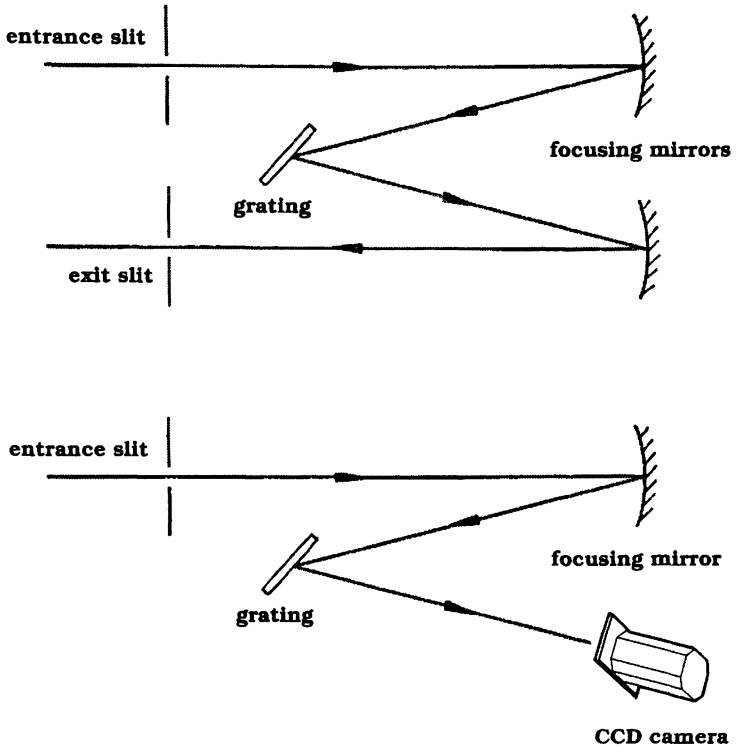

Figure 3.2: Layout of the classical (top) and the modified (bottom) Czerny-Turner configuration. The classical arrangement is in essence a monochromator, imaging a single wavelength onto the exit slit. A spectrum is obtained by rotating the grating. On the other hand, the modified configuration used in this thesis simultaneously images a range of wavelengths.

Light from a 12° circular field of view is transmitted through an order-sorting filter and enters the spectrometer via a 45 mm arc-length, curved Fastie slit. The curved slit reduces astigmatism inherent in linear slits. An adjustable slit width of 0.5 mm provides a good compromise between throughput and spectral resolution. A 0.5-m focal length spherical mirror collimates the incoming rays and reflects the light onto a movable, 110 mm × 110 mm, 1200 grooves/mm plane diffraction grating, blazed at 1000 nm. The grating disperses the light into a spectrum which is then focused on the CCD detector by an $f/1.4$, 85-mm focal length compound lens. An Andor DU420-BR-

DD CCD camera with 1024 × 256, 26 μm square pixels, optimized for measurements in the near-infrared, images the spectra. The CCD chip is thermoelectrically cooled; this, in conjunction with an external recirculated-liquid cooling unit, allows operating temperatures down to $-110°$ C. At this temperature, the peak quantum efficiency of the detector is ~90%, and the dark current is 0.15 electrons/pixel/s. The slowest readout rate of 33 kHz (with an associated noise of 4 electrons/pixel) was employed. A low operating temperature (low dark current), and slow readout rate (decreased noise), led to high signal-to-noise (S/N) ratios, and facilitated the detection of weak emission features.

When observing in first order, the spectrometer covered a free spectral range of ~180 nm, and imaged spectral lines had a nominal full width at half maximum (FWHM) of about 0.8 nm. However, the resolution at longer wavelengths was impaired by a focusing problem with the CCD lens.

3.3 Experiment details

The High Power Auroral Stimulation (HIPAS) 2007 Optics Campaign was carried out from 7–20 March 2007. Observations presented in Chapter 4 were obtained during the nights of 19 and 20 March 2007, under clear skies. Geomagnetic conditions were quiet: Kp was 1− and 0+ on the 19$^{\text{th}}$, and 0 on the 20$^{\text{th}}$ For the 24 hours preceding both days, $Kp \leq 1+$. Absorption was negligible, as evinced by double-hop echoes on Digisonde profiles obtained from College, 50 km away (see Figure 3.3). During the period of brightest optical emissions, f_oF_2 was ~3.5 MHz. For both nights, the spectrometer was pointed up-**B**, and observing in first order, from ~700 to 880 nm.

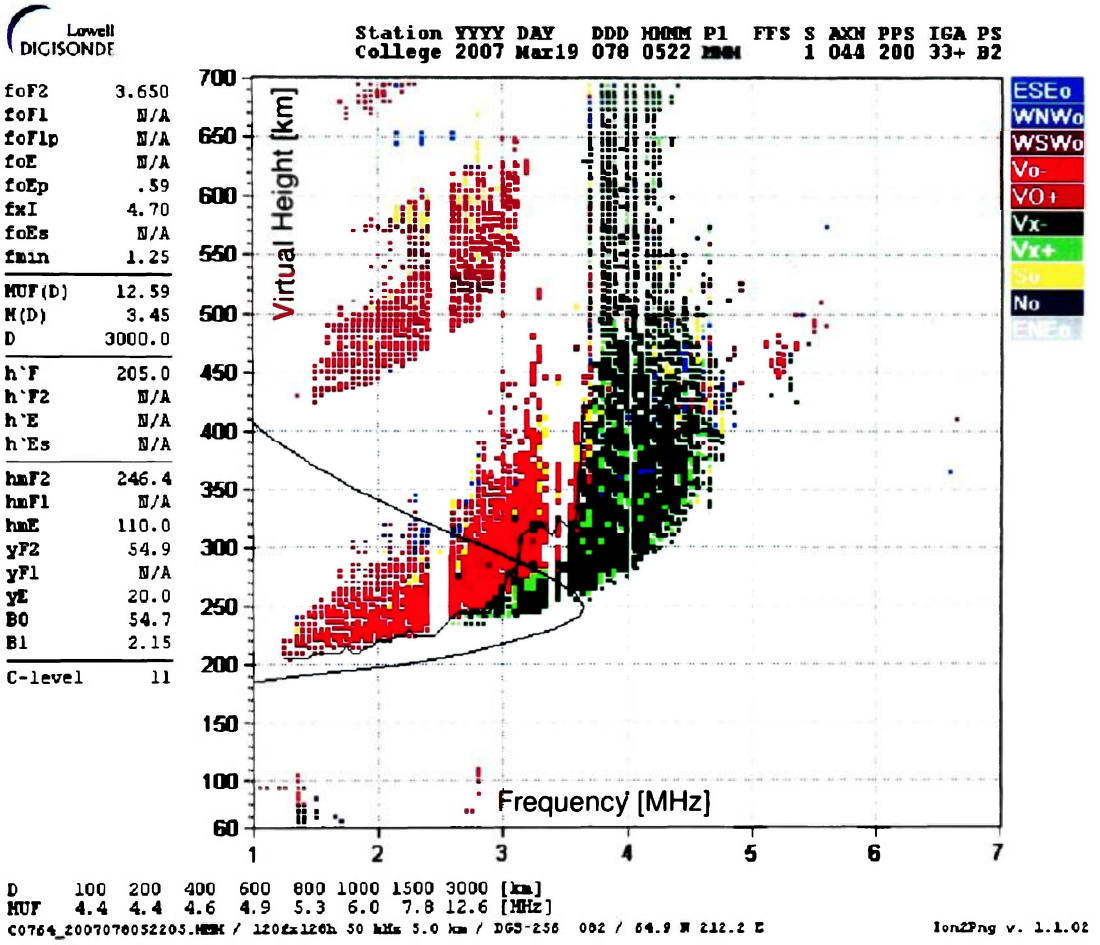

Figure 3.3: A Digisonde profile obtained during the experiment on 19 March 2007. Double-hop echoes attest to negligible ionospheric absorption of the pump wave. Magenta and green returns are from o- and x-mode polarizations, respectively. The black line is an estimate of the true height profile.

3.3.1 Heater duty cycle

The heater alternated between pointing along the field line (up-**B**) over both HIPAS (χ=13°, azimuth=204°) and Poker Flat Research Range (PFRR, dip angle χ=13°, azimuth=246°). Both of these beam positions were outside the Spitze cone (~7.5°). Continuous wave (CW), o-mode polarization at a fixed frequency of 2.85

MHz was used on both nights. When heating up-**B** over HIPAS, the total transmitter power was 588 kW; an antenna gain of 17.39 dB yielded an ERP of 32 MW.

19 March 2007

Figure 3.4 shows the heater duty cycle as a function of time. Starting at 0424 UT (2024 local time), the heater ran in a 6 min cycle: 50 ms pulses every 4 s for 2 min, pointed above PFRR; 2 min of continuous wave, up-**B** over HIPAS; followed by 2 min off. At 0612 UT, the heating above PFRR was changed to 50 ms pulses every 1 s.

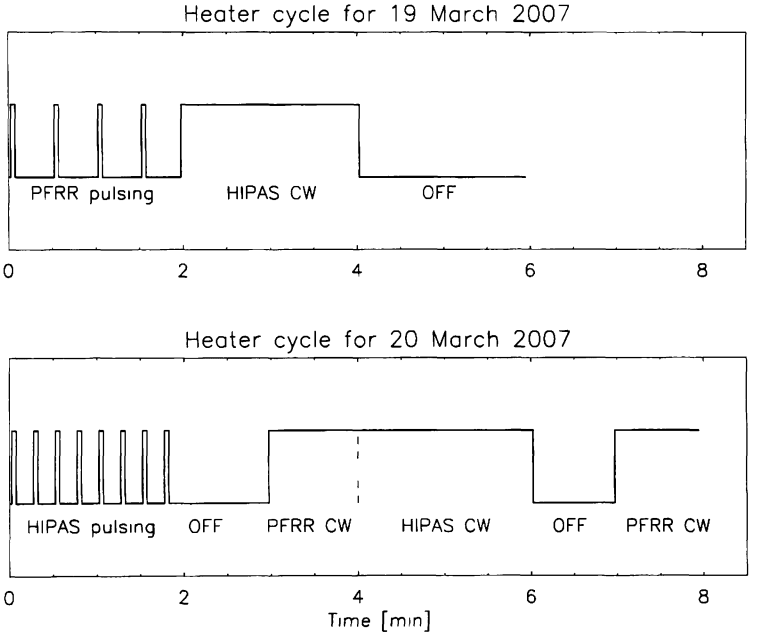

Figure 3.4: The heater cycle for the nights of 19 and 20 March 2007. The pulses during the initial 2 minutes are either 50 ms or 100 ms long.

20 March 2007

On this night, HIPAS was heating in an 8 min cycle. Beginning at 0522 UT (2122 local time), the pump beam was stepped through the following sequence: 2 min of 50 ms pulsed heating at a frequency of 1 Hz up-**B** over HIPAS, followed by 1 min off. Next was 1 min of CW heating up-**B** over PFRR, then 2 min of CW heating up-**B** over HIPAS, another 1 min off, and the cycle was completed with 1 min of CW heating up-**B** over PFRR. At 0538 the pulses above HIPAS were lengthened to 100 ms.

3.4 Data analysis

The top panel in Figure 3.5 shows a raw CCD image acquired at 0550 UT on 19 March 2007. The image is 1024 $\times$ 64 pixels; vertical on-chip binning of every 4 rows increased the S/N, and also reduced the readout time, permitting longer exposures. The rounded nature of the spectral lines is an artifact of the curved slit employed. To accurately determine the wavelength, and to enable co-adding of the rows, it is necessary to eliminate the curvature of the spectral lines. This is achieved as follows: a fiducial row close to the center of the image is selected, since the curvature of the lines is smallest here. Next, a cross-correlation between all the rows and the fiducial row, with a range of lag values, is performed. Each row is then shifted by the lag value that maximizes the cross-correlation. The resulting image is displayed in the lower panel of Figure 3.5. A plot of the fiducial row and the co-added spectrum from the same CCD image are shown in Figure 3.6. The co-added spectra is an average of the response across the CCD chip. Applying the same procedure to the spectrum of a gas discharge lamp with known spectral lines allows each pixel to be mapped to a specific wavelength, thus enabling an accurate wavelength calibration.

Figure 3.5: Upper panel: a raw CCD image, as recorded by the spectrometer. The curvature of the spectral lines is an artifact of the curved entrance slit. Lower panel: the curvature-corrected image.

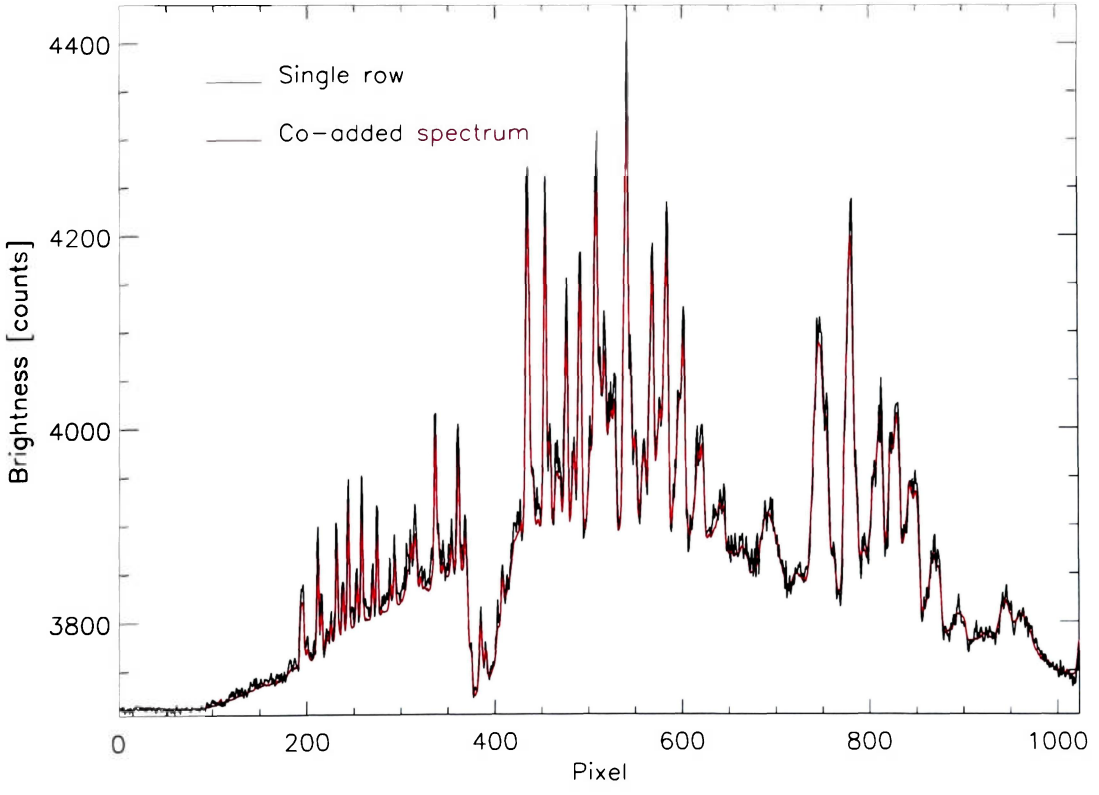

Figure 3.6: A row plot (black) and the co-added spectrum (red) from a single CCD image.

In order to improve the S/N, it was necessary to co-add not just the rows of a single image, but the spectra too. Additionally, weak emissions generated by a heater are often indiscernible in a single heater-on spectrum, but require a subtraction of the heater-off spectrum. Below I enumerate the procedure used to obtain the radio-induced emissions presented in the following chapter.

1. Three successive heater-on spectra and three successive heater-off spectra were averaged to obtain composite spectra. Only CW and off pulses above HIPAS were used.

2. The off spectrum was subtracted from the on spectrum, yielding a difference spectrum.

3. The difference spectrum was separated into bins surrounding wavelengths of candidate RIOEs.

4. A calibration was applied to each bin, enabling the brightness of any observed RIOEs to be calculated (further details on the absolute intensity calibration are provided in Appendix A).

5. The minimum value of the difference spectrum was set to zero, since random noise in the spectra could produce negative brightness values.

6. Standard deviations were calculated for bins showing significant emission peaks.

To the best of my knowledge, no previous spectroscopic time series data, showing optical emission modulation by a heater, exists in the literature. As mentioned in Chapter 2, previous detections of RIOEs are almost without exception limited to all-sky cameras and photometers. The time series data of RIOEs provided in Chapter 4 were obtained from the heater-on and heater-off spectra as follows:

1. A range of pixels corresponding to possible RIOEs was selected. For line emissions, this was typically 2-4 pixels.

2. The total intensity of the emission feature was obtained by summing across this range, for both the heater-on and heater-off spectra.

3. The airglow intensity during each on and off period is divided by the intensity during the off period, yielding a ratio R_i, which for enhanced emissions is $>$ 1 during the on periods, and is always 1 during the off periods. This ratio is referred to as the normalized optical intensity. Note that the heater on/off intensity values need not be calibrated.

4. The degree of "correlation" between the heater cycle and the emission enhancement during the time series is obtained by calculating the quantity $C = \Sigma(R_i - 1)$, summing over all the on and off periods. Clearly, an unenhanced emission has $R_i \simeq 1$ and thus $C \approx 0$. Conversely, an emission modulated by the heater would be expected to have $R_i > 1$, and $C > 0$, the magnitude of C depending on the extent of the modulation.

The time series is not strictly continuous, since the spectrometer was sighted up-**B**, and only the CW and off pulses above HIPAS were included. The effective heater duty cycle on the 19^{th} was thus 2 min CW up-**B** over HIPAS, 2 min off. On the 20^{th}, the effective heater duty cycle was 2 min CW up-**B** over HIPAS, followed by 1 min off. In order to facilitate a meaningful comparison between the on and off exposures, the optical emission time series for the 20^{th} was generated as follows: the 2 min on period consisted of two 1 minute exposures. Since the heater-off period was only 1 min long, the first minute of the heater-on period is compared to the heater-off exposure, and the second minute of the heater-on exposure is also compared to the same heater-off

exposure.

Chapter 4

Results

> "What we are trying to do is determine the size of these wiggles."
>
> Dr Hughes

Figure 4.1a presents sample spectra recorded by the spectrometer. The wavelength-dependent full width half maximum (FWHM) of the spectral lines was 0.6−2 nm, with the resolution at longer wavelengths impaired by a focusing problem with the CCD lens. Prominent emission features include the OH Meinel (8,3), (9,4), (5,1) and (6,2) bands starting at 727, 775, 791, and 834 nm respectively. Also visible are the O_2 Atm. (0,0) band centered at 762 nm, and the O_2 Atm. (0,1) band at 859 nm. The red spectrum is an average of 3 consecutive up-**B** scans over HIPAS at 0544, 0550, and 0556 UT, while the black spectrum is an average of 3 consecutive heater-off scans (0546, 0552, and 0558 UT). It should be noted that the heater-induced O^+ and O emissions underlie brighter spectral features and are indiscernible in Figure 4.1a. The difference in brightness between the on and off spectra is not a heater-induced effect but is simply a changing background caused by the setting Sun.

Figure 4.1b−d shows background-subtracted, calibrated difference spectra in 10 nm bins surrounding the O^+ 732−733 nm, $O(^5P)$ 777.4 nm, and $O(^3P)$ 844.6 nm emissions.

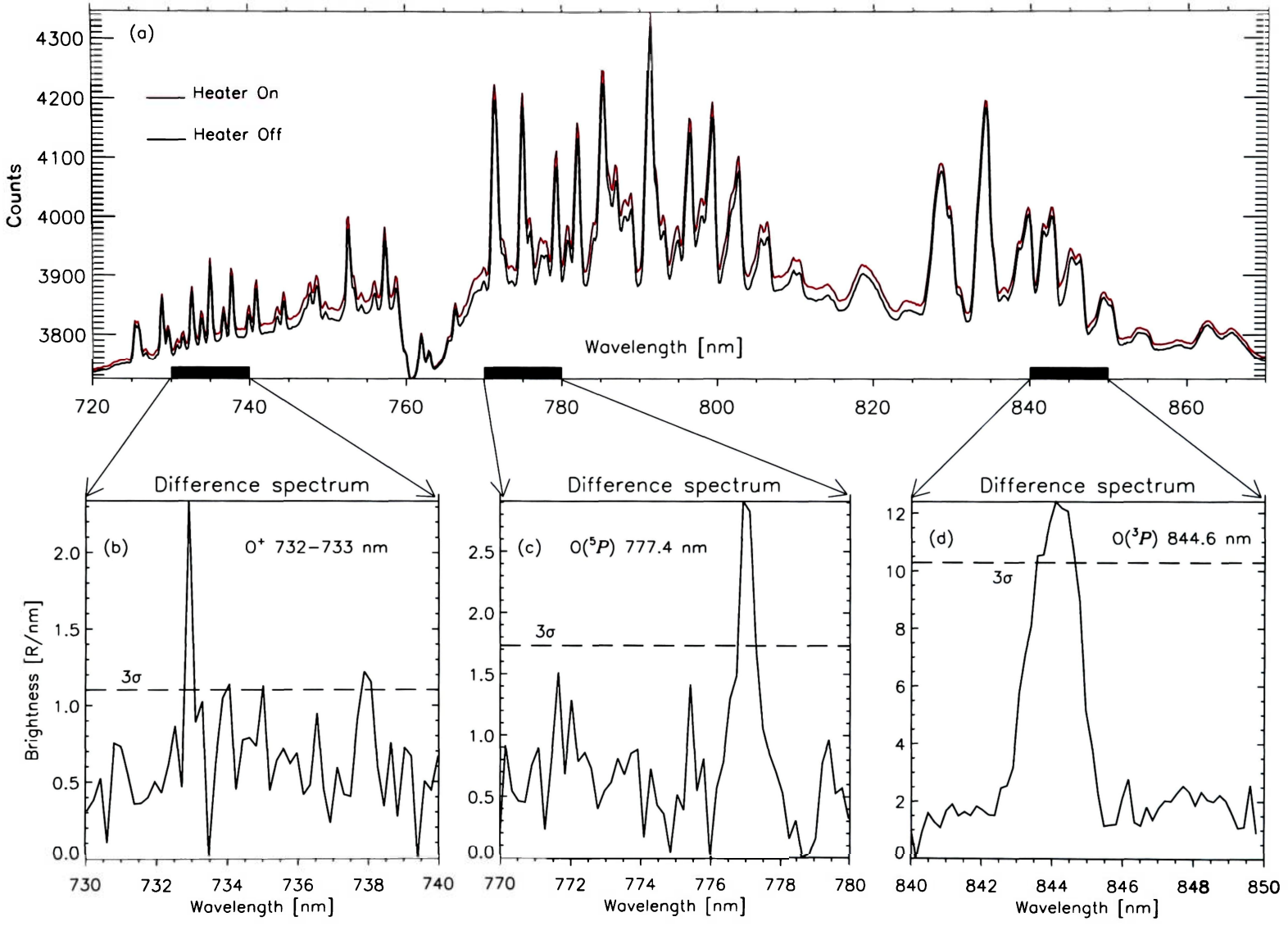

Figure 4.1: Airglow emissions recorded at HIPAS. (a) Sample spectra obtained during heater-on (red) and heater-off (black) periods. Radio-induced optical emissions discussed in the text underlie brighter spectral features in the highlighted ranges. (b)–(d) Background-subtracted, calibrated difference spectra, showing radio-induced optical emissions at selected regions of interest.

The emission peaks clearly stand out above the noise level. Displayed as a horizontal dashed line is the 3σ standard deviation of the signal (99.7% confidence level) for each range. 52, 53, and 57 data points were used in the standard deviation calculations for the 732.0 nm, 777.4 nm, and 844.6 nm bins, respectively. The observed brightness is in R/nm, and as discussed later, the O(^5P) 777.4 nm and O(^3P) 844.6 nm values are similar to previous results obtained by *Djuth et al.* [2005] and *Gustavsson et al.* [2005].

Figure 4.2 further illustrates the presence of RIOEs. Figure 4.2a is a time series of the ionospheric critical frequency, f_oF_2. The horizontal dashed line denotes the heater pump frequency, f_h, and the 2nd gyroharmonic, $2f_{ce}$, at 2.85 MHz. Plus symbols (+) and diamond symbols ($\diamond$) in Figure 4.2b show the altitudes of the plasma resonance layer (PRL) and the upper hybrid resonance layer (UHRL), respectively. The PRL corresponds to the altitude at which the plasma frequency, f_p, matches the heater frequency. The UHRL, which on average was 12 km below the PRL, is the altitude where upper hybrid waves [e.g., *Hughes et al.*, 2003] are generated.

Also shown in Figure 4.2b is the 2nd gyroharmonic altitude at ~245 km, as determined from the IGRF10 model. The diagonal line represents the solar terminator altitude, and thus demarcates the shadow height. The vertical lines 1 and 2 mark the plasma resonance and double resonance conditions, which occurred at ~0613 UT and ~0633 UT, respectively.

Time series of background-subtracted, normalized optical intensities, plotted in conjunction with the heater duty cycle, are presented in Figure 4.2c–g. Heating pulses above Poker Flat Research Range are not included. For this experiment, the O(^3P) 844.6 nm and the O(^5P) 777.4 nm emissions (Figure 4.2c–d) show the highest correlation. The O^+ 732–733 nm and the O($^3D^o$) 799.0 nm (Figure 4.2e–f) display a somewhat weaker correlation, but modulation by the heater is still evident. Lastly,

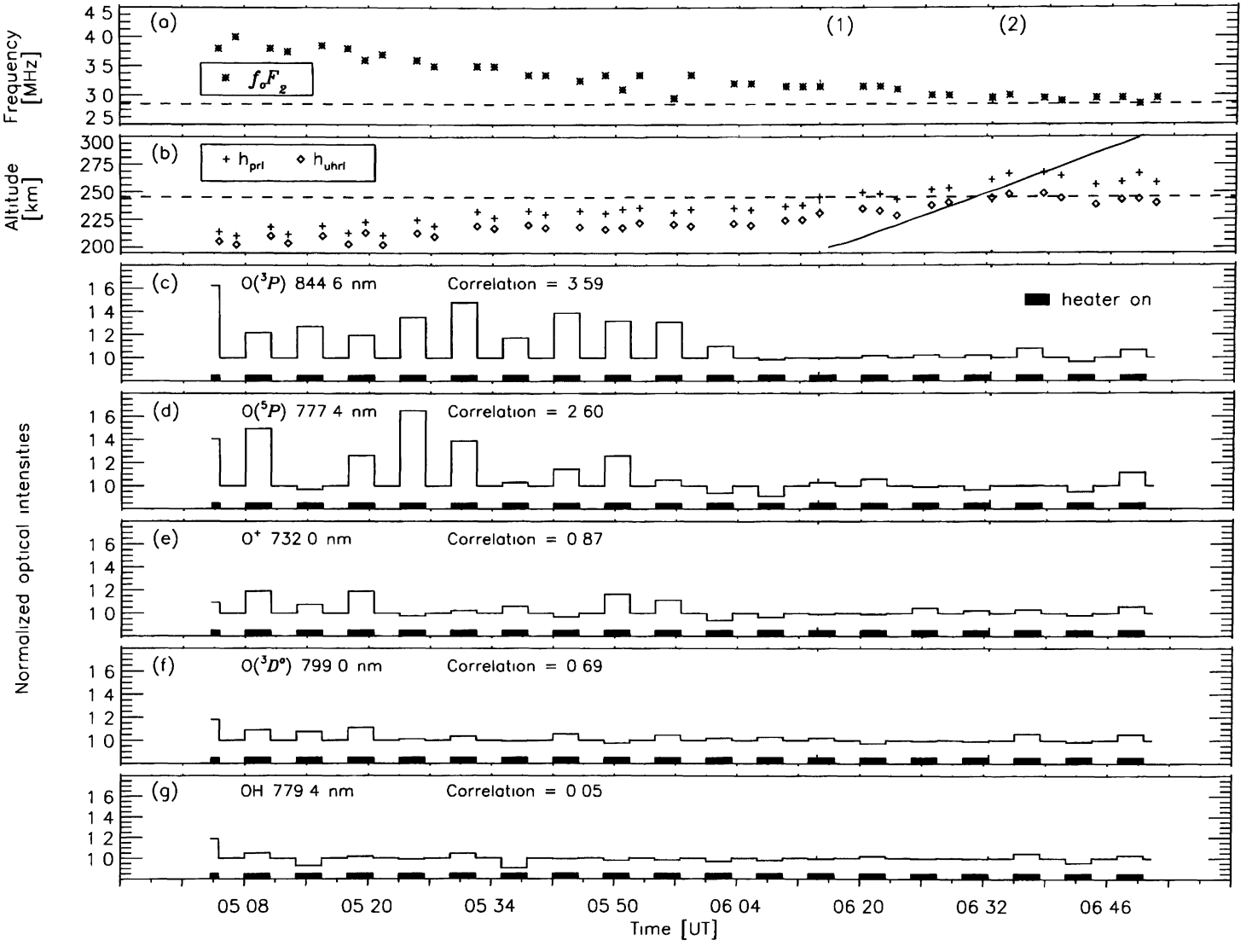

Figure 4.2: Ionospheric parameters and optical emission time series for 19 March 2007 (a) f_oF_2 The horizontal dashed line denotes the heater pump frequency and the 2nd gyroharmonic, $2f_{ce}$ (b) Plasma resonance (+) and upper hybrid resonance (◇) layers The horizontal line at ~245 km indicates the 2nd gyroharmonic altitude The diagonal line demarcates the shadow height Vertical lines (1) and (2) correspond to the plasma resonance (~0613 UT) and double resonance (~0633 UT) conditions (c)–(g) Background-subtracted, normalized optical intensities plotted in conjunction with the heater duty cycle

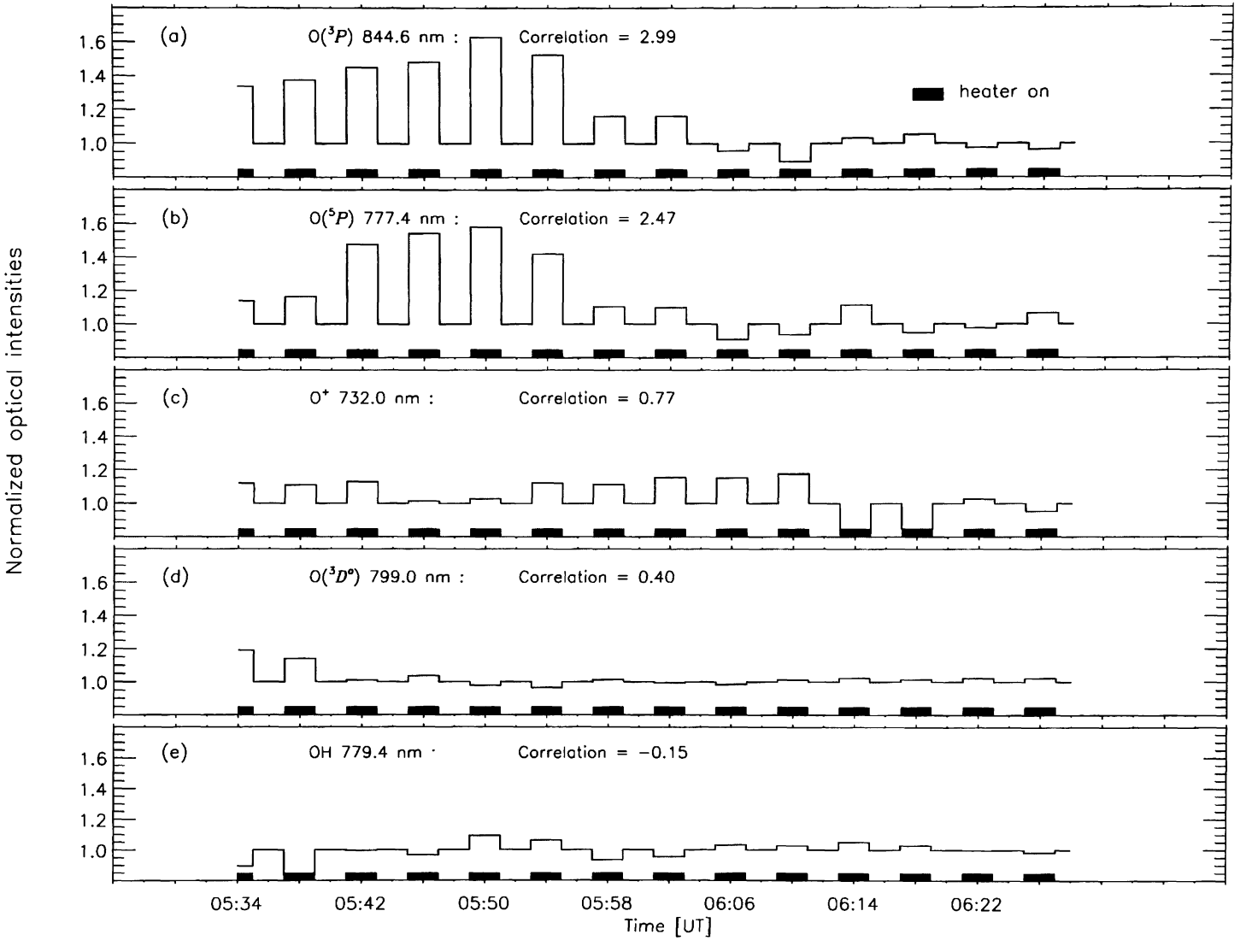

Figure 4.3: Background-subtracted, normalized optical intensities for the night of 20 March 2007, plotted in conjunction with the heater duty cycle.

the $P_1(2)$ line of the OH(9,4) band at 779.4 nm (Figure 4.2g) shows a very low correlation and a lack of modulation by the heater.

Concurrent ionospheric parameters were unavailable for 20 March 2007, due to an instrument malfunction. Figure 4.3 presents a time series of background-subtracted, normalized optical intensities for that night. Modulation of the $O(^3P)$, $O(^5P)$ and O^+ emissions is clearly evident.

4.1 Discussion of results

We have presented the first spectroscopic time series observations of a heated volume, showing RIOE modulation by the heater. In addition, this marks the first detection of the O^+ 732.0−733.0 nm and $O(^3D^o)$ 799.0 nm emissions during ionospheric heating. These data were acquired during a two week heating campaign at the HIPAS heating facility. Only two nights, 19th and 20th March 2007, yielded good results. The confluence of conditions required for the successful generation of optical emissions (clear, dark skies, sufficient ionospheric plasma, quiet geomagnetic activity, low absorption, and a suitable heating mode) usually limits the number of days with good optical data. Also, during periods close to solar minimum, the window between dark skies and $f_oF_2 \gtrsim f_h$ is short. This often leads to experiments being performed in twilight conditions, with a large solar background present.

Figure 4.1 shows that, without further analysis, the spectrum of the heated volume during the on and off periods appears identical. However, as mentioned before, the heater-induced O^+ and O emissions are weak and underlie brighter spectral features, requiring a differencing in order to ascertain the presence of RIOEs.

Observed RIOEs in Figure 4.1 had intensities between 2−25 R. How do these values compare with other observations? In a cusp aurora, where the range of electron

energies is more similar to that observed during ionospheric heating than in the nightside aurora, intensities of up to 150 R for the O^+ are not uncommon [*Sivjee et al.*, 1999]. This is higher than our observations, but no prior measurements from heating experiments are available. Previous detections of the $O(^3P)$ [*Gustavsson et al.*, 2005] and $O(^5P)$ [*Djuth et al.*, 2005] during ionospheric heating have yielded intensities of ~15 R and <10 R, respectively. Our detection of 25 R for $O(^3P)$ and ~2 R for $O(^5P)$ is therefore comparable to prior observations.

The metastable O^+ 732−733 nm multiplet emission arises out of the $O^+(^2P^o) \rightarrow O^+(^2D^o)$ transition. Under auroral conditions, the $(^2P^o)$, $(^2D^o)$ and the (ground) $(^4S^o)$ states are produced according to equation 4.1, in fractions of 0.2, 0.4 and 0.4, and requiring 18.61, 16.92, and 13.61 eV respectively [*Rees*, 1989].

$$O + e \longrightarrow 2e + O^+(^2P^o, {}^2D^o, {}^4S^o) \tag{4.1}$$

Photoionization gives rise to the emission in the twilight airglow spectrum [*Meriwether et al.*, 1978], and given the position of the terminator in Figure 4.2b, it is apparent that our observed emissions were obtained from above the shadow height ($O(^5P)$ and $O(^3P)$ also occur naturally in the dayglow). Nevertheless, the data presented in Figure 4.2c−f show clear modulations by the heater. Furthermore, twilight conditions produce suprathermal photoelectrons, and consequently, larger numbers of already-energetic electrons are available for acceleration than is possible with a Maxwellian distribution. We therefore propose that either (or both) of $O^+(^4S^o) \rightarrow O^+(^2P^o)$, requiring 5.00 eV, or $O^+(^2D^o) \rightarrow O^+(^2P^o)$ (1.69 eV), was caused by heater-induced electron acceleration and subsequent impact excitation of O^+ The reaction $O + e \rightarrow 2e + O^+(^2P^o)$ (18.61 eV) cannot be ruled out, since *Gustavsson et al.* [2006] and *Holma et al.* [2006] have both observed heater-induced N_2^+ 427.8 nm, which

requires 18.75 eV.

The O^+ 732.0−733.0 nm emission spectra can be contaminated by the $P_1(2)$ and the $P_2(3)$ lines of the OH(8,3) band, and by auroral N_2 1P (5,3). The latter can be discounted on the basis that electron energies hard enough to produce N_2 emissions would have led to markedly different spectra. In addition, a 630.0 nm imager with a detection threshold of 3.5 R acquired simultaneous airglow images which showed no background aurora. Regarding possible OH contamination of the O^+ 732−733 nm, the $P_1(2)$ line of the OH(9,4) band at 779.4 nm shows no modulation by the heater (Figure 4.1g). Thus, we expect no heater-induced modulation of the $P_1(2)$ and the $P_2(3)$ lines of the OH(8,3) band. More significantly, OH production peaks at ~87 km, over 100 km lower than the interaction altitudes determined here, and the only report of heater-induced OH emissions is by *Kagan et al.* [2005], who observed an enhancement from the E region. We can therefore safely assume negligible OH modulation by the heater, and hence no contamination should be present in the difference spectra.

The 799.0 nm multiplet is a weak auroral emission generated by the $O(^3D^o) \rightarrow O(^3P)$ transition. It contributes significantly via cascade excitation to the $O(^3P)$ 844.6 nm emission, and in bright aurora its intensity is ~1% of the $O(^1S)$ 557.7 nm green line [*Christensen et al.*, 1983]. The only possible significant source of contamination for this emission, and also for $O(^3P)$ 844.6 nm and $O(^5P)$ 777.4 nm, is OH, which we have addressed above.

The question might be asked why only emissions from O and O^+ were detected during the heating. A simple and logical explanation is that the PRL and UHRL shown in Figure 4.2b lie in the altitude range where O and O^+ are prevalent, and therefore emissions from these species should be expected. A similarity is once again drawn between emissions observed during heating, and those present during cusp

(dayside) aurora, which are also primarily from O and O^+.

We now turn to the optical time series presented in Figures 4.2 and 4.3. With the onset of nightfall and the decay of the ionosphere, the critical frequency f_oF_2 dropped, as shown in Figure 4.2a. This led to a lifting of the plasma and upper hybrid resonance layers; since the heater wave had to propagate further into the ionosphere to encounter sufficient plasma to meet the matching conditions. As a consequence, the interaction altitudes were almost entirely in sunlit conditions.

Overall, the 844.6 nm and 777.4 nm emissions, Figure 4.2c–d display the strongest correlation to the heater (the correlation coefficient, C, partly attests to this, but is also biased toward brighter emissions). The two emissions follow a similar pattern with their intensities peaking at roughly the same time. This pattern is repeated for both nights. The O^+ 732–733 nm is not as well correlated as the 844.6 nm and 777.4 nm emissions, and displays a minima in intensity coincident with the maxima displayed by the latter two. This is more pronounced on the 20^{th}, and might suggest a softening of the electron energy spectrum, possibly due to preferential development of one of the RIOE production mechanisms. Unfortunately, this cannot be further explored with the available data.

The correlation coefficient, C, is smaller for all the emissions on the 20^{th}, but this is due to a shorter time series ($\sim$50 min as opposed to $\sim$100 min on the 19^{th}). C is calculated for the entire time series, even though it is evident that RIOE production stops soon after 0600 UT on both days. After this, the number of on/off pairs with $R_i < 1$ is large compared to before 0600 UT. This emphasizes that before 0600 UT, all the emissions with the exception of OH are modulated by the heater. ($R_i < 1$, corresponding to RIOE intensity during heater-off > heater-on, can be expected in the absence of heater modulation or a sustained increase or decrease in emission intensity).

Djuth et al. [2005]; *Kosch et al.* [2005]; *Mishin et al.* [2005] and *Kosch et al.* [2007a], among others, have presented data showing significant increases in optical emission brightness when the plasma resonance (Figure 4.2b, vertical line 1, ~0613 UT) and double resonance (vertical line 2, ~0633 UT) conditions were met. This is a well-established phenomena during heating experiments close to $2f_{ce}$. At plasma resonance, $f_p = 2f_{ce} = f_h$. Similarly, the double resonance condition is satisfied when $f_{uh} = 2f_{ce} = f_h$, that is, when the heater frequency matches the second gyroharmonic, at the upper hybrid resonance altitude. It is noteworthy that no increase in RIOE production was observed close to the resonance conditions; in fact, the brightest emissions occurred approximately 1 hr before double resonance. Simultaneous 630.0 nm and 557.7 nm observations display the same behavior (*Todd Pedersen, personal communication*).

Ionospheric parameters were obtained from hand-fitted ionograms, which introduce a ±10 km uncertainty in calculated ionospheric altitudes [*Kosch et al.*, 2005]. Nevertheless, taking this uncertainty into account would shift the plasma resonance to 0550 UT at the earliest, and the double resonance to 0618 UT. This would still be later than the period of maximum optical response starting at ~0530 UT. In addition, any uncertainty due to the geographic separation of the Digisonde and the heater (1° longitude, ~85 km at F-region heights) is expected to be less than the ±10 km uncertainty introduced by the ionograms. This is because the observations were carried out during quiet geomagnetic conditions and close to the terminator passage, so to first order the density gradients should be following the Sun. Thus, an uncertainty of about 4 minutes in the ionospheric parameters can be attributed to the geographic separation of the heater and the Digisonde; this still puts the maximum optical emissions outside the plasma resonance–double resonance window. Ionospheric parameters for the night of the 20th might have shed light on why the

expected increase in RIOEs did not occur at plasma resonance and double resonance.

Given the pump frequency used and the timing of the emissions with respect to the various resonances, there are several candidate mechanisms that could have generated the observed RIOEs. Chiefly, the parametric decay of the pump wave into Langmuir (L) and ion acoustic (IA) waves, PDI_L, is a well-known occurrence that efficiently accelerates electrons via Langmuir turbulence [*Fejer*, 1979]. This mechanism has been theoretically predicted by *Gurevich et al.* [2002] for pumping outside the Spitze cone ($\sim$7.5° at HIPAS), and ample experimental evidence exists [e.g., *Kosch et al.*, 2007a, and references therein]. Also plausible is that the parametric decay (PDI_{EB}) of the pump wave into electron Bernstein (EB) waves and lower hybrid (LH) waves [e.g., *Mishin et al.*, 2005; *Kosch et al.*, 2007a] was in effect. The likely presence of suprathermal photoelectrons would have enhanced the airglow production of both mechanisms.

Chapter 5

Concluding Remarks

The ionosphere, which is the ionized component of our atmosphere, forms the gateway between Earth and the interstellar medium. The Sun, apart from sustaining life on our planet, is also the dominant driver of Earth's weather. As such, knowledge of ionospheric processes and properties is important in the study of the Sun-Earth system. One clear and captivating manifestation of the Sun's effect on our atmosphere is the aurora. This thesis has presented spectroscopic observations of artificially induced aurora detected during a $2f_{ce}$ ionospheric heating experiment. The expected increase in optical emission intensity close to the resonance conditions, borne out by previous experiments, was not observed in this work and is an unexpected result requiring further study. Indeed, the words of *Walker* [1979] still seem true today: there is a failure of theory to predict phenomena before they are observed. Equally true, however, is a paucity of observations to test current theories. Therefore, to better characterize the artificial aurora production mechanisms and the responses of various emissions to these mechanisms, additional theory and observations are required.

Spectroscopic observations, when compared to photometric and all-sky observations, are generally faced with poor temporal resolution due to their reduced

throughput. To improve on this, a faster spectrometer is desired. The increased throughput would enable acquisition of spectra with comparable (or better) S/N levels as the current instrument, but with exposure times of ~10s of seconds. Ratios of observed RIOEs could then be used to determine the temporal evolution of the heater-accelerated electron energy spectrum with increased resolution. Analysis of high temporal and spatial resolution optical data, in combination with measurements from coherent and incoherent scatter radars, would illuminate the complex wave-plasma interactions that occur during ionospheric heating. To this end, the ramping up of solar activity, and the planned upgrades at HAARP, making it the only $2f_{ce}$ heater with a full complement of diagnostic equipment, augur well for the field of ionospheric heating.

Appendix A

Absolute Intensity Calibration

Absolute intensity calibration of the CCD spectrometer was performed with a blackbody and a Lambertian screen. The blackbody is an energy source of known spectral brightness, with a calibration traceable to the National Institute of Standards and Technology (NIST). When illuminated by the blackbody, the Lambertian screen diffuses incident radiation and ensures that the apparent brightness recorded by the spectrometer is independent of observing angle. The arrangement is shown in Figure A.1.

The energy output of the blackbody for a particular temperature and aperture area can be precisely determined. With a knowledge of the blackbody-to-screen distance and the screen reflectivity, one can calculate the theoretical brightness of the Lambertian screen (in R/nm). The ratio of this theoretical brightness to the spectrometer's response when viewing the screen is a calibration factor that determines the spectral response of every pixel on the CCD detector. The product of the calibration curve [R/nm/count] and acquired spectra [counts] yields calibrated spectra from which the brightness of observed emissions [R/nm] is obtained. Figure A.2 is a plot of absolute intensity calibration curves. §3.5 details the wavelength calibration procedure.

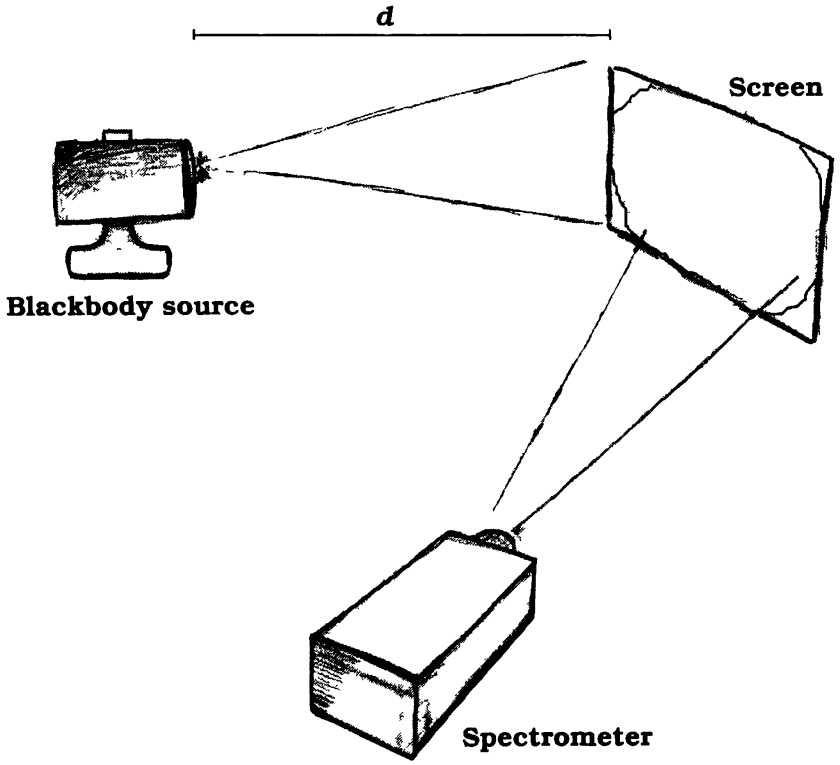

Figure A.1: Physical layout of the calibration setup. The blackbody source is perpendicular to the screen, at a sufficient distance away, d, that the reflected radiation fills the field of view of the spectrometer.

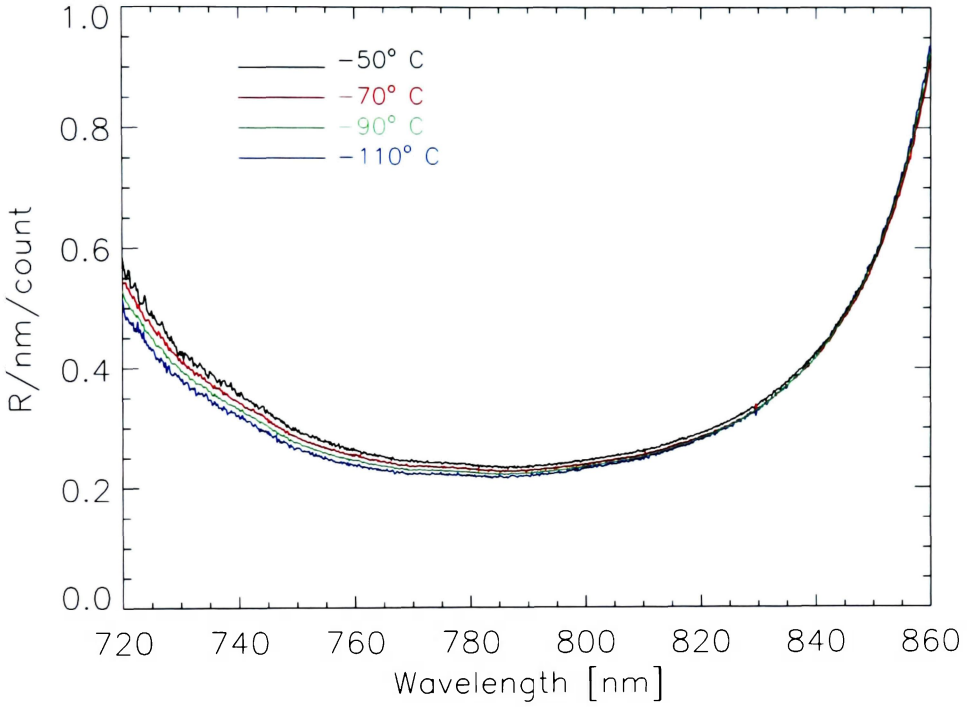

Figure A.2: Calibration curves (from a single row), showing the CCD detector's response at four different temperatures. Airglow emissions presented in Chapter 4 were recorded in Alaska, with a CCD temperature of −110° C. To accurately determine the brightness of the observed emissions, a calibration performed at the same CCD temperature is required. However, the warmer ambient temperature in the laboratory where the calibration was performed precluded cooling of the CCD to lower than −90° C. Therefore, the calibration curve at −110° C is an interpolation of three calibrations performed at −50° C, −70° C and −90° C. For all the calibrations, the following parameters were used: blackbody temperature, 1000° C; blackbody-to-screen distance, 34.50 in. Two calibrations were performed at each temperature, using blackbody aperture diameters of 0.100 in. and 0.200 in.; these were averaged to obtain the above curves.

Appendix B

CCD Camera Data Acquisition Software

The following Andor Basic code, running on an Andor MCD version 4.1 and Windows XP SP2 platform, was used to control the DU420-BR-DD CCD camera. Other than the CCD temperature, identical camera settings were used during the calibrations. Due to a large increase in dark counts (present only in Alaska), the CCD fan was turned off during data acquisition.

```
//use this during the heating.
//*************** Program BEGINS here ****************
cls()
//*********user selectables*****************************
EPOCH = 0.0
DURATIONONMIN = 1.0            // HIPAS duty cycle on in MINUTES
DURATIONOFFMIN = 1.0           // HIPAS duty cycle off in MINUTES
TEMPERATURE = -120             // temperature in C
YBIN = 4                       // horizontal binning
XFLIP = 1                      // this reverses the xscale and
                               // saves it in increasing wavelength
NoAcqs = 300                   // acquisitions to acquire
root$="c:\data\hipas\mar 20\a"

//*********end user selectables************************
```

```
cls()
DURATIONONSEC = DURATIONONMIN * 60  // HIPAS duty cycle on in sec
DURATIONOFFSEC = DURATIONOFFMIN * 60 // HIPAS duty cycle off (sec)
?" "
?"HIPAS duty cycle: ";str$(DURATIONONSEC);"seconds ON,
                    ";str$(DURATIONOFFSEC);"seconds OFF"
?"*****************************************************"
acq=1
while(acq<=NoAcqs)
        gosub .GetTime
        t = min + (sec/60.)
        st = EPOCH
        while (st <= t)
                st = st + DURATIONONMIN
                et = st + DURATIONOFFMIN
                if (st <= t) then
                        st = st + DURATIONOFFMIN
                        et = et + DURATIONONMIN
                endif
                //print ("here",t,st,et)
                if( st > 60. ) then st=0.
        wend
        EXPOSURE = ((et - st)*60.0) - 15  // 15s to save file
        if( st >=60 ) then st=st-60.
        if( et >=60 ) then et=et-60.
        gosub .SetupExpt    // Configure data acquisition setup
        gosub .StartExpt    // Wait until START TIME
        gosub .GetFilename
        ?" "
        ?"Just about to run, time is ";time$()
        ?"*********************************"
        run()               // Acquire data
        gosub .SaveAcq      // Save data to hard disk
        acq=acq+1
wend

?" "
?"Experiment completed at time ";time$()
?"*************************************"
end
//*************** main program ENDS here **************
```

```
//**************** Subroutines begin here **************

//**************** SetupExpt  *************************
//acquisition parameters

.SetupExpt

// Temperature
        SetTemperature(TEMPERATURE)
        cooler(1)

//Acquisition
        //SetAcquisitionMode(1)         // obsoleted by SetSingleScan
        //SetReadoutMode(4)             // obsoleted by setImage
        SetImage(1,1024,1,1,256,YBIN,XFLIP,0)
                // (hstart,hend,hbin,vstart,vend,YBIN,xflip,yflip)
        SetSingleScan(EXPOSURE)         // this is the exposure
                                        // duration in sec
        SetAcquisitionType(0)           // signal
        SetDataType(1)                  // counts
        SetReadoutTime(64.25)           // in usec

//Shutter
        SetTriggerMode(0)               // internal
        SetShutter(2,1)                 // shutter is auto, TTL
                                        // high to open (default)
        SetShutterTransferTime(10)      // 10 ms (default)
        Showtimings()

//windows
        //MinimizeWindow(#0)
        //MinimizeWindow(program)
return

//********************** StartExpt**********************
//.StartExpt will only be exited once the seconds match StartTime

.StartExpt
        gosub .GetTime
        now = min + (sec/60.) + (msec/60000.)
                while ( (now < st) or ((now-st)>30) )
                        delay(100)   // delay for 100 millisec
```

```
                        gosub .GetTime
                        print (now,st,et)
                        now = min + (sec/60.)
                wend
return

//**************** GetTime  ***************************
//time format is (eg) 18:15:23.05

.GetTime
        timestring$=time$()
        h$=left$(timestring$,2)         // hours
        m$=mid$(timestring$,4,2)        // minutes
        s$=mid$(timestring$,7,2)        // seconds
        ss$=right$(timestring$,2)       // seconds/100
        fracss$=left$(ss$,1)            // first digit of
                                        // millisec to build filename.

        hour = val(h$)
        if (hour < 10) then
                h$ = "0";str$(hour)
        endif
        //print(h$,hour)
        min = val(m$)
        sec = val(s$)
        msec= val(ss$)
        print (timestring$,h$,m$,s$,ss$,fracss$)
return

//**************** GetFilename  ************************
//Generate filename string...make filename beginning of scan

.GetFilename

        today$ = date$()
        if (strcomp(mid$(today$,2,1), "/")) then
                    // enters if double digit month
                if (strcomp(mid$(today$,5,1),"/")) then
                                // enters if double digit day
                        mth$ = left$(today$,2)
                        day$ = mid$(today$,4,2)
                else                // single digit day
```

```
                        mth$ = left$(today$,2)
                        day$ = "0";mid$(today$,4,1)
                endif

        endif
        if (strcomp(mid$(today$,3,1), "/")) then
                        // single digit month
                if (strcomp(mid$(today$,4,1),"/")) then
                        // enters if double digit day
                        mth$ = "0";left$(today$,1)
                        day$ = mid$(today$,3,2)
                else        // single digit day
                        mth$ = "0";left$(today$,1)
                        day$ = "0";mid$(today$,3,1)
                endif

        endif
        year$ = right$(today$,2)
      //print(today$)
      //print(mth$,day$,year$)
        gosub .GetTime          //get latest values of time
        filename$ = root$;year$;mth$;day$;h$;m$;".";s$;fracss$
        print(filename$)        //this is printed out at
                                //      beginning of scan
        BeginTime$ = time$()    //place this in the header
return

//**************** SaveAcq  ****************************

.SaveAcq

        EndTime$ = time$()      // for header...end of scan...
                                // this includes write out time
        Export32(#0,filename$)
        xsize=imagex(#0)        // obtain image sizes for header
        ysize=imagey(#0)
        a=write(filename$,xsize)
        if a<0 then
                print("Error on write")
        endif
        write(filename$,ysize)
        write(filename$,YBIN)
```

```
        write(filename$,XFLIP)
        write(filename$,today$)
        write(filename$,BeginTime$)
        write(filename$,EndTime$)
        write(filename$,EXPOSURE)
        write(filename$,TEMPERATURE)  // should use $gettemperature
        close()
        //stracq$ = "#";str$(acq)
        //print(stracq$)
        //CloseWindow(stracq$)
return
//**************** End subroutines ****************************
```

References

Adeishvili, T. G., A. V Gurevich, S. B. Lyakhov, G. G. Managadze, G. M. Milikh, and I. S. Shlyuger (1978), Ionospheric emission caused by intense radio wave, *Sov. J. Plasma Phys.*, *4*, 721–726.

Bahsoun-Hamade, F., R. H. Wiens, and G. G. Shepherd (1994), Thermospheric O I 844.6-nm emission in twilight, *J. Geophys. Res.*, *99*(A4), 6289–6295.

Bailey, V. A., and D. F Martyn (1934), Influence of electric waves in the ionosphere, *Phil. Mag.*, *18*, 369–386.

Baumjohann, W., and R. A. Treumann (1997), *Basic Space Plasma Physics*, Imperial College Press, Singapore.

Bernhardt, P., C. Tepley, and L. Duncan (1989), Airglow enhancements associated with plasma cavities formed during ionospheric heating experiments, *J. Geophys. Res.*, *84*, 9071–9092.

Bernhardt, P. A., M. Wong, J. D. Huba, B. G. Fejer, L. S. Wagner, J. A. Goldstein, C. A. Selcher, V. L. Frolov, and E. N. Sergeev (2000), Optical remote sensing of the thermosphere with HF pumped artificial airglow, *J. Geophys. Res.*, *105*(A5), 10,657–10,671.

Biondi, A. A., D. P. Sipler, and R. D. Hake, Jr (1970), Optical (λ6300) detection of radio frequency heating of electrons in the F region, *J. Geophys. Res.*, *75*(31), 6421–6424.

Brändström, B. U. E., T. B. Leyser, Å. Steen, M. T. Rietveld, B. Gustavsson, T. Aso, and M. Ejiri (1999), Unambiguous evidence of HF pump-enhanced airglow at auroral latitudes, *Geophys. Res. Lett.*, *26*, 3561–3564.

Budden, K. G. (1985), *The propagation of radio waves*, Cambridge University Press, Cambridge, United Kingdom.

Carlson, H. C., Jr, and L. M. Duncan (1977), HF excited instabilities in space plasmas, *Radio Sci.*, *12*(6), 1001–1013.

Chamberlain, J. W. (1961), *Physics of the aurora and airglow*, Academic Press Inc, New York, United States.

Christensen, A. B., M. H. Rees, G. J. Romick, and G. G. Sivjee (1978), The O I (7774 Å) and O I (8446 Å) emissions in aurora, *J. Geophys. Res.*, *83*(A4), 1421–1425.

Christensen, A. B., G. G. Sivjee, and J. H. Hecht (1983), O I (7990 Å) emission and radiative entrapment of auroral EUV, *J. Geophys. Res.*, *88*(A6), 4911–4917.

Djuth, F. T., T. R. Pedersen, E. A. Gerken, P. A. Bernhardt, C. A. Selcher, W. A. Bristow, and M. J. Kosch (2005), Ionospheric modification at twice the electron cyclotron frequency, *Phys. Rev. Lett.*, *94*, 125001, doi:10.1103/PhyRevLett.94.125001.

Erdman, P. W., and E. C. Zipf (1983), Electron impact excitation of λ7990 Å multiplet, *J. Geophys. Res.*, *88*(A9), 7245–7249.

Erdman, P. W., and E. C. Zipf (1987), Excitation of the OI ($3s\,^5S^0 - 3p\,^5P$; λ7774 Å) multiplet by electron impact on O_2, *J. Chem. Phys*, *87*(8), 4540–4545.

Evans, W. F. J., E. J. Llewellyn, J. C. Haslett, and L. R. Megill (1970), Preliminary results from the 1.27-micron measurements in the Boulder ionospheric modification experiment, *J. Geophys. Res.*, *75*(31), 6425–6428.

Fejer, J. (1979), Ionospheric modification and parametric instabilities, *Rev. Geophys.*, *17*, 135–153.

Gerdjikova, M. G., and G. G. Shepherd (1987), Evaluation of the auroral 5577-Å excitation process using Intercosmos Bulgaria 1300 satellite measurements, *J. Geophys. Res.*, *92*(A4), 3367–3374.

Gombosi, T. I. (1998), *Physics of the space environment*, Cambridge University Press, New York, United States.

Gordon, W. E., and H. C. Carlson, Jr (1974), Arecibo heating experiments, *Radio Sci.*, *9*(11), 1041–1047.

Grach, S. M., N. A. Mityakov, V. O. Rapoport, and V. Y. Trakhtengertz (1981), Thermal parametric turbulence in a plasma, *Physica D (Amsterdam)*, *2*, 102–106.

Gurevich, A. V., H. Carlson, and K. P. Zybin (2001), Nonlinear structuring and southward shift of a strongly heated region in ionoshperic modification, *Phys. Lett. A*, *288*, 231–239.

Gurevich, A. V., K. P. Zybin, H. C. Carlson, and T. Pedersen (2002), Magnetic zenith effect in ionospheric modifications, *Phys. Lett. A*, *305*, 264–274.

Gustavsson, B., T. B. Leyser, M. Kosch, M. T. Rietveld, Å. Steen, B. U. E. Brändström, and T. Aso (2006), Electron gyroharmonic effects in ionization and electron acceleration during high-frequency pumping in the ionosphere, *Physical Review Letters*, *97*(19), 195002, doi:10.1103/PhysRevLett.97.195002.

Gustavsson, B., et al. (2001), First tomographic estimate of volume distribution of HF-pump enhanced airglow emission, *J. Geophys. Res.*, *106*(A12), 29,105–29,123.

Gustavsson, B., et al. (2005), The electron distribution during HF pumping, a picture painted with all colors, *Ann. Geophys.*, *109*, 1747–1754.

Haslett, J. C., and L. R. Megill (1974), A model of the enhanced airglow excited by RF radiation, *Radio Sci.*, *9*(11), 1005–1019.

Hecht, J. H., A. B. Christensen, and J. B. Pranke (1985), High-resolution auroral observations of the OI(7774) and OI(8446) multiplets, *J. Geophys. Res.*, *12*(9), 605–608.

Henriksen, K., W. Stoffregen, B. Lybekk, and Å. Steen (1984), Photometer and spectrometer search of the oxygen green and red lines during artificial ionospheric heating in the auroral zone, *Ann. Geophys.*, *2*(1), 73–76.

Holma, H., K. U. Kaila, M. J. Kosch, and M. T. Rietveld (2006), Recognizing the blue emission in artificial aurora, *Adv. Space Res.*, *38*(11), 2653–2658.

Honary, F., T. R. Robinson, D. M. Wright, A. J. Stocker, and M. T. Rietveld (1999), First direct observations of the reduced striations at pump frequencies close to the electron gyroharmonics, *Ann. Geophys.*, *17*, 1235–1238.

Hughes, J. M., W. A. Bristow, R. T. Parris, and E. Lundell (2003), SuperDARN observations of ionospheric heater-induced upper hybrid waves, *Geophys. Res. Lett.*, *30*(24), 2276, doi:10.1029/2003GL018772.

Hughes, J. M., W. A. Bristow, and R. T. Parris (2004), SuperDARN observations of spectral enhancements excited during an ionospheric heating experiment, *Geophys. Res. Lett.*, *31*, L08808, doi:10.1029/2004GL019613.

Hunsucker, R. D., and J. K. Hargreaves (2003), *The high-latitude ionosphere and its effects on radio propagation*, Cambridge University Press, Cambridge, United Kingdom.

Istomin, Y. N., and T. B. Leyser (1995), Parametric decay of an electromagnetic wave near electron cyclotron harmonics, *Phys. Plasmas*, *2*, 2084–2097.

Istomin, Y. N., and T. B. Leyser (2003), Electron acceleration by cylindrical upper hybrid oscillations trapped in density irregularities in the ionosphere, *Phys. Plasmas*, *10*(7), 2962–2970.

Kagan, L. M., et al. (2005), Observation of radio-wave-induced red hydroxyl emission at low altitude in the ionosphere, *Phys. Rev. Lett.*, *94*, 095004, doi: 10.1103/PhysRevLett.94.095004.

Kosch, M. J., M. T. Rietveld, T. Hagfors, and T. B. Leyser (2000), High-latitude HF induced airglow displaced equatorwards of the pump beam, *Geophys. Res. Lett.*, *27*, 2817–2820.

Kosch, M. J., M. T. Rietveld, A. J. Kavanagh, C. Davis, T. K. Yeoman, F. Honary, and T. Hagfors (2002), High-latitude pump-induced optical emissions for frequencies close to the third electron gyro-harmonic, *Geophys. Res. Lett.*, *29*(23), doi:10.1029/2002GL015744.

Kosch, M. J., M. T. Rietveld, F Honary, and T. Hagfors (2003), High-latitude artificial aurora from EISCAT: A unique phenomenon?, *Sodankylä Geophysical Observatory*, *92*, 7–10.

Kosch, M. J., M. T. Rietveld, A. Senior, I. W. Mcrea, A. J. Kavanagh, B. Isham, and

F. Honary (2004), Novel artificial optical annular structures in the high lattitude ionosphere, *Geophys. Res. Lett.*, *29*, L12805, doi:10.1029/2006GL019713.

Kosch, M. J., T. Pedersen, J. Hughes, R. Marshall, E. Gerken, A. Senior, D. Sentman, M. McCarrick, and F. T. Djuth (2005), Artificial optical emissions at HAARP for pump frequencies near the third and second electron gyro-harmonic, *Ann. Geophys.*, *23*, 1585–1592.

Kosch, M. J., T. Pedersen, E. Mishin, S. Oyama, J. Hughes, A. Senior, B. Watkins, and B. Bristow (2007a), Coordinated optical and radar observations of ionospheric pumping for a frequency pass through the second electron gyroharmonic at HAARP, *J. Geophys. Res.*, A06325, doi:10.1029/2006JA012146.

Kosch, M. J., T. Pedersen, M. T. Rietveld, B. Gustavsson, S. M. Grach, and T. Hagfors (2007b), Artificial optical emissions in the high-latitude thermosphere induced by powerful radio waves: An observational review, *Adv. Space Res.*, *40*, 365–376.

Lundborg, B., and B. Thidé (1986), Standing wave pattern of HF radio waves in the ionospheric reflection region 2. Applications, *Radio Sci.*, *21*(3), 486–500.

Meriwether, J. W., Jr, D. G. Torr, J. C. G. Walker, and A. O. Nier (1978), The $O^+(^2P)$ emission at 7320-Å in twilight, *J. Geophys. Res.*, *83*(A7), 3311–3319.

Mishin, E., T. Hagfors, and B. Isham (2001), A generation mechanism for topside enhanced incoherent backscatter during high frequency modification experiments in Tromsø, *Geophys. Res. Lett.*, *28*, 479–482.

Mishin, E. V., M. J. Kosch, T. Pedersen, and W. J. Burke (2005), HF-induced

airglow at magnetic zenith: Thermal and parametric instabilities near electron gyroharmonics, *Geophys. Res. Lett.*, *32*, L23106, doi:10.1029/2005GL023864.

Mjølhus, E. (1990), On linear conversion in a magnetized plasma, *Radio Sci.*, *25*(6), 1321–1339.

Mjølhus, E. (1993), On the small scale striation effect in ionospheric radio modification experiments near harmonics of the electron gyrofrequency, *J. Atmos. Terr. Phys.*, *55*, 907.

Mjølhus, E., and T. Flå (1984), Direct access to plasma resonance in ionospheric radio experiments, *J. Geophys. Res.*, *89*(A6), 3921–3928.

Mutiso, C. K., J. M. Hughes, G. G. Sivjee, T. Pedersen, B. Gustavsson, and M. J. Kosch (2008), Previously unreported optical emissions generated during ionospheric heating, *Geophys. Res. Lett.*, *35*(14), L14103, doi:10.1029/2008GL034563.

Pedersen, T., and E. A. Gerken (2005), Creation of visible artificial optical emissions in the aurora by high-power radio waves, *Nature*, *433*, 498–500.

Pedersen, T. R., and H. C. Carlson (2001), First observations of HF heater-produced airglow at the High Frequency Active Auroral Research Program facility: Thermal excitation and spatial structuring, *Radio Sci.*, *36*(5), 1013–1026.

Pedersen, T. R., M. McCarrick, E. Gerken, C. Selcher, D. Sentman, H. C. Carlson, and A. Gurevich (2003), Magnetic zenith enhancement of HF radio-induced airglow production at HAARP, *Geophys. Res. Lett.*, *30*(4), 1169, doi: 10.1029/2002GL016096.

Rees, M. H. (1989), *Physics and chemistry of the upper atmosphere*, Cambridge University Press, Cambridge, United Kingdom.

Rietveld, M T , H Kohl, H Kopka, and P Stubbe (1993), Introduction to ionospheric heating at Tromsø – I Experimental overview, *J Atmos Solar-Terr Phys* , *55*(4/5), 577–599

Robinson, T R (1989), The heating of the high latitude ionosphere by high power radio waves, *Physics Reports*, *179*, 79–209

Sandholt, P E , H C Carlson, and A Egeland (2002), *Dayside and polar cap aurora*, Kluwer Academic Publishers, Dordrecht, The Netherlands

Sergienko, T , I Kornilov, E Belova, T Turunen, and J Manninen (1997), Optical effects in the aurora caused by ionospheric HF heating, *J Atmos Solar-Terr Phys* , *59*, 2401–2407

Sipler, D P , and M A Biondi (1972), Measurements of O(^{1}D) quenching rate in the *F* region, *J Geophys Res* , *77*, 6202–6212

Sipler, D P , E Enemark, and M A Biondi (1974), 6300-Å intensity variations produced by the Arecibo ionosphere modification experiment, *J Geophys Res* , *79*, 4276–4280

Sivjee, G G , G J Romick, and M H Rees (1979), Intensity ratio and center wavelengths of [O II] (7320-7330 Å) line emissions, *Astrophys J* , *229*, 432–438

Sivjee, G G , A B Christensen, K Henriksen, and A E Belon (1984), OI 7774 A and 8446 A emissions from the night-side and midday cusp auroras, *Ann Geophys* , *2*, 463–466

Sivjee, G G , D Shen, J -H Yee, and G J Romick (1999), Variations, with peak emission altitude, in auroral O_2 atmospheric (1,1)/(0,1) ratio and its relation to other auroral emissions, *J Geophys Res* , *104*(A12), 28,003–28,018

Smith, R. W., G. G. Sivjee, R. D. Stewart, F. G. McCormac, and C. S. Deehr (1982), Polar cusp ion drift studies through high-resolution interferometry of O^+ 7320 Å emission, *J. Geophys. Res.*, *87*(A6), 4455–4460.

Solomon, S. C., P. B. Hays, and V J. Abreu (1988), The auroral 6300 Å emission: observations and modelling, *J. Geophys. Res.*, *93*(A9), 9867–9882.

Stubbe, P., et al. (1982), Ionospheric modification experiments in northern Scandinavia, *J. Atmos. Terr. Phys.*, *44*(12), 1025–1041.

Swanson, D. G. (2003), *Plasma waves, 2nd edition*, Institute of Physics Publishing, Bristol, United States.

Walker, J. C. G. (1979), Active experimentation with the ionospheric plasma, *Radio Sci.*, *17*(4), 534–544.

Wygant, J. R., et al. (2000), Polar spacecraft based comparisons of intense electric fields and Poynting flux near and within the plasma sheet-tail lobe boundary to UVI images: An energy source for the aurora, *J. Geophys. Res.*, *105*(A8), 18,675–18,692.